The Effect of Liquid Film on Cavity Filling

Ankit Kumar

Technische Universiteit Delft

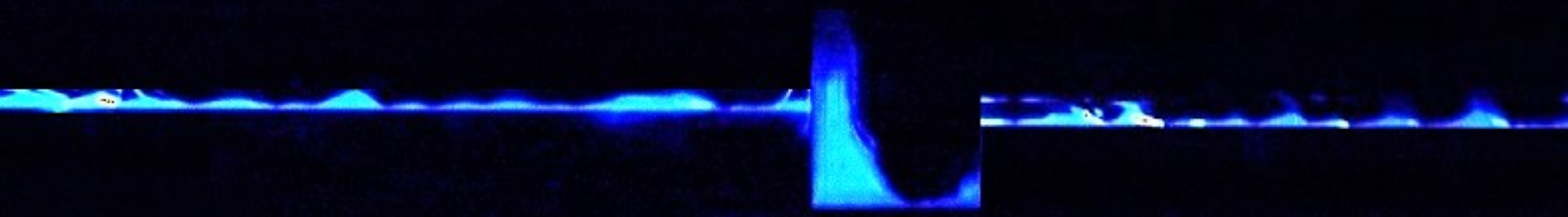

TU Delft

The Effect of Liquid Film on Cavity Filling

by

Ankit Kumar

to obtain the degree of Master of Science
at the Delft University of Technology,
to be defended publicly on Thursday March 29, 2018 at 02:00 PM.

Student number:	4507681	
P&E report number:	2889	
Project duration:	January 15, 2017 – March 29, 2018	
Supervisors:	Prof. dr. ir. C. Poelma,	TU Delft
	Ir. A.C. van Eckeveld,	TU Delft
	Ir. M. van Meerkerk,	TU Delft
Thesis committee:	Dr. ir. J.T. Padding,	TU Delft

TU Delft Delft University of Technology

Acknowledgements

This thesis marks the end of my studies at TU Delft. The past year has been a very challenging as well as rewarding experience for me and wouldn't have been possible without the help and guidance from a lot of people.

First and foremost, I am grateful to Prof. Christian Poelma for giving me the opportunity to work on this project and for all his critical feedbacks during our meetings. I would like to extend my deepest thanks to my daily supervisors Andries and Mike, for their help throughout the duration of this thesis and for always being approachable. Their enthusiasm and encouragement during our meetings always kept me going. I would also like to thank Dr. Johan Padding for taking time out and agreeing to be a part of my thesis committee. Further, I want to extend my sincere gratitude to the support staff of the Aero and Hydro lab, who helped me with setting up my experiments. In particular, I would like to thank Jasper for manufacturing my experimental model, Jan for his help with the electrical equipment and Edwin for helping me with the laser and optics.

I would also like to thank the PhD students of the lab and my fellow students in the Master's room for the coffee breaks, discussions and small talks we had. A special thanks to my classmates from SPET; Diggie, Adi and Abhiroop for all the memorable discussions we had, and making my time in the lab very enjoyable.

My time in Delft wouldn't have been as fun if it were not for Dab, Sabya, Sagar, Manni and Kislay. I cherished the evenings we spent together. I would also like to thank Bikku bhaiya, bhabhi and my *lief* niece Vania. Even after being so far away from home, I always felt at home when I visited them in the weekends.

Lastly, I want to thank my parents and my sister, for their unconditional love and support. I am eternally grateful to them for supporting me in my decision to study abroad and for their constant encouragement throughout my studies.

Ankit Kumar
Delft, March 2018

Abstract

Noise generated due to flow over corrugated pipes has extensively been studied, because of its presence in various engineering applications. Flexible risers used in the oil and gas industry are one of these applications, where noise is produced due to corrugations present at the innermost layer of the riser. Dry-gas flow through a corrugated pipe generates an unstable shear layer over each of the corrugations. Under certain conditions, this shear layer can roll up into discrete vortices, which impinge on the downstream cavity edge, producing pressure pulsations. When the frequency of impingement matches with one of the natural pipe frequencies, a 'lock-in' mechanism causes intensification of the associated noise and vibrations, which can have serious implications on the structural integrity of the corrugated pipe. This phenomenon is called *Flow Induced Pulsations* (FIP). Liquid injection in a corrugated pipe with gas flow has shown the potential to mitigate whistling caused by FIP. A number of mechanisms play a role in the whistling mitigation. It is shown in literature that the filling of cavities due to liquid film or rivulets present on the pipe wall is an important mechanism. The cavity filling results in an altered cavity geometry, which changes the shear layer dynamics. The effect of liquid and gas flow rate on the cavity filling, however, remains unknown. The present work aims to study the liquid filling behaviour of a single cavity, due to a gas flow driven liquid film.

An experimental setup is constructed which consists of a rectangular channel containing a cavity. Liquid is injected in the channel as a film at the channel wall, which is driven upward by gas flow. The liquid film thickness upstream of the cavity is measured first, followed by the cavity filling itself. Both measurements are performed using a Laser Induced Fluorescence (LIF) based technique. After several post-processing steps, the film thickness and cavity filling are quantified.

At low liquid flow rates, a partial film is created at the channel wall with a dry patch at the center. Increasing the liquid flow rate results in a full film covering the entire channel width. The film thickness varies in the transverse direction due to the presence of localized horseshoe shaped disturbance waves on the liquid film. Overall, the film cross-sectional area increases with increasing liquid flow rate, either due to an increase in film thickness of full films, or an increase in width of the partial films. The liquid film fills up the cavity, accumulating mainly at the upstream edge. The downstream edge remains relatively free from liquid. The amount of filling is found to increase with increasing local film thickness at the measurement position away from the channel side-wall. Changes in the cavity geometry due to liquid filling are estimated based on the cavity effective depth and length. The effective cavity depth does not significantly change and only decreases by 8% with a 25% increase in filling ratio. However, the effective length decreases substantially by 30% with a 25% increase in filling ratio. This could lead to a mode parameter value (ratio of cavity length to incoming gas momentum thickness), such that it does not fall in the range where whistling is observed, resulting in mitigation of whistling.

Contents

List of Figures

List of Tables

Glossary

Acronyms

FIP	Flow induced pulsations	
JIP	Joint industry project	
LIF	Laser induced fluorescence	

List of Symbols

α	Cavity filling ratio	
$\bar{\delta}$	Mean film thickness	m
δz	Depth of field	m
δ	Liquid film thickness	m
δ_{99}	Boundary layer 99% thickness	m
δ_*	Boundary layer displacement thickness	m
λ_f	Wavelength of fluorescent light	Hz
λ_l	Wavelength of laser light	Hz
ϕ_l	Liquid volume fraction	
ρ_g	Gas density	$\mathrm{kg/m^3}$
ρ_l	Liquid density	$\mathrm{kg/m^3}$
σ	Surface tension per unit length	N/m
σ_δ	Standard deviation in film thickness	m
θ	Boundary layer momentum thickness	m
θ_c	Critical angle for total internal reflection	°
A	Area of rectangular channel	$\mathrm{m^2}$
$c_1,\ c_2$	Pressure transducer calibration constants	Pa
D_c	Cavity depth	m

D_h	Hydraulic diameter of rectangular channel	m
D_r	Distance between opposite plates of rectangular channel	m
D_{eff}	Effective cavity depth	m
E	Voltage output from pressure transducer	V
f	Frequency of impingement of shear layer vortices	Hz
$f_{\#}$	F-stop of camera lens	
IN	Inertial force	N
L_c	Cavity length	m
L_{eff}	Effective cavity length	m
$M_\circ$	Camera magnification	
Ma	Mach number	
n	Mode of oscillation	
P	Perimeter of rectangular channel	m
p_{dyn}	Dynamic pressure	Pa
p_{static}	Static pressure	Pa
p_{total}	Total pressure	Pa
Q_g	Gas volume flow rate	L/min
Q_l	Liquid volume flow rate	L/min
Re	Reynolds number	
ST	Surface tension force	N
St	Stouhal number	
U_g	Gas bulk velocity	m/s
$U_{g,loc}$	Local gas velocity	m/s
W_c	Cavity width	m
W_r	Width of rectangular channel	m
We	Weber number	
x	Flat plate streamwise distance	m

1

Introduction

1.1. Background

In the oil and gas industry, the transport of the hydrocarbons produced from the sea floor to an offshore platform is done through risers. Besides transport, risers are also used for drilling, as well as for water and chemical injection flow lines. Earlier, risers were simple rigid steel pipes. But with the offshore sites moving to deeper waters, harsher conditions and highly dynamic environment, the need for risers to be flexible arose and flexible risers started replacing conventional rigid risers. Flexible risers have been in use for over 30 years worldwide, in a number of fields including West Africa, the Gulf of Mexico, the North Sea and Brazil [1, 2].

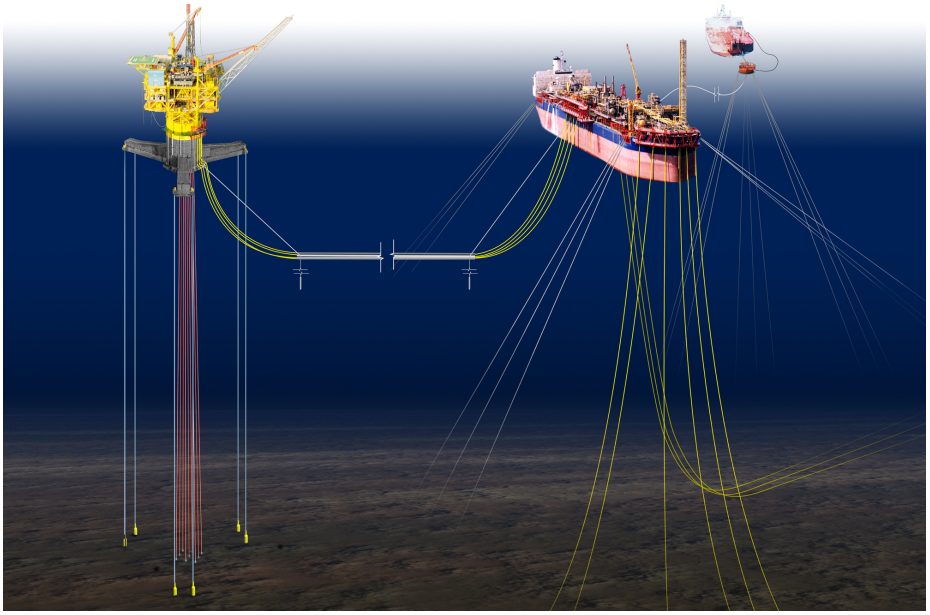

Figure 1.1: Risers (in yellow) connected to the sea bed and the offshore site (rigzone.com, 2014).

Risers often have to bear high temperatures in the range of $150°C$, high fluid pressure of up to 400 bars, depths up to 2500 m and constant contact with corrosive materials [1]. Hence they are made of a number of layers each of which serves a specific purpose (eg., withstanding high internal and external fluid pressures, wear resistance and flexibility). The different layers of a typical riser are shown in Figure 1.2. The flexibility is provided by the innermost layer, called carcass, due to the presence of corrugations across the perimeter of the riser. These corrugations allow the risers to have a global flexibility, while maintaining local rigidity.

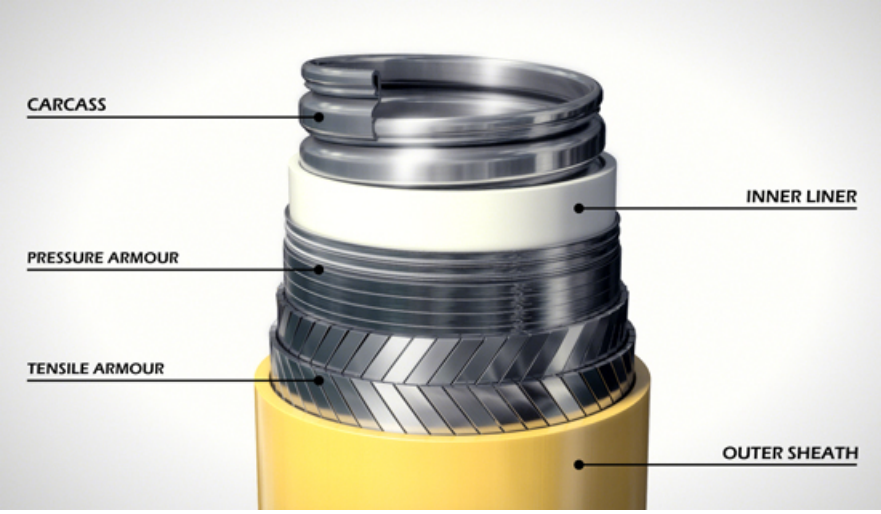

Figure 1.2: Different layers of a riser (pangeranlaut.wordpress.com, 2016).

1.2. Motivation

Flexible risers have a complex design as compared to their rigid pipe predecessors. These additional complexities make them more susceptible to failure. Some of the reasons for failure of the riser structure include [3]:

- *Fatigue* in the thin steel ribbons of the carcass which may progress to other layers, leading to a pipe failure. This can occur due to inaccurate fabrication or varying load conditions.
- *Corrosion* in the armour wires, when they are exposed to seawater due to damage to the outer sheath.
- *Collapse* of the pressure liner and carcass caused by an external pressure exceeding the load limit of the carcass.
- *Erosion* of the carcass due to sand and hydrates in the flow.

Reports from the Petroleum Safety Authority, Norway show around 1.5% probability of failure per riser per operational year for the Norwegian offshore sector [2]. Although the percentage is small in absolute terms, it is still significant considering the catastrophic repercussions a riser failure can have on human lives and the environment.

With increasing demands for natural gas, more satellite wells are being connected to existing subsea infrastructure, leading to higher gas velocities in the associated piping [4]. This has lead to a new possible failure mode of flow induced pulsations (FIP). FIP results in distinctive tonal noise, high flow resistances and vibrations leading to potential fatigue failure at the topside and subsea piping. Because of the whistling sound it produces, the risers showing this behaviour are often referred to as 'singing risers'. Since this phenomenon occurs only above certain gas velocity, the reactive mitigation measure to prevent further failure has been to reduce the rate of gas export. But, this is not a feasible solution given that the gas demands are only expected to rise [5].

A joint industry project (JIP) called 'Flexible Risers' was thus initiated, co-funded by international oil and gas companies to pro-actively investigate the technical issues associated with this singing behaviour [6]. Through comprehensive field and laboratory experiments, as well as numerical simulations, the JIP has thoroughly investigated the causes and characteristics of whistling risers [6]. The tonal noise produced due to gas flow through corrugated pipes has long been a topic of research and is abunduntly found in literature [7–9]. In the case of flexible risers, the innermost layer called carcass is responsible for the noise production. The carcass is made up of a number of corrugations, which can be thought of as alternate cavities and plateaus at the surface of the pipe. A part of the carcass containing a single cavity is shown in Figure 1.3.

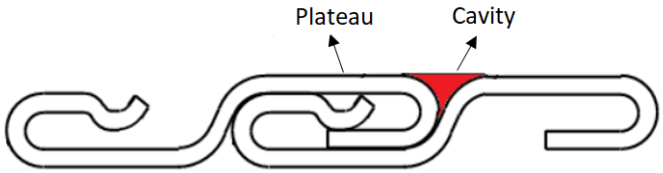

Figure 1.3: An example of the riser carcass geometry. Adapted from [10].

When gas flows over these cavities, flow separation occurs at the upstream edge of each cavity generating an unstable shear layer. This shear layer can roll-up into vortices, as shown in Figure 1.4, which impinge on the downstream edge, resulting in pressure fluctuations. If the frequency of the impingement of these vortices over individual cavities matches a natural frequency of the riser, a resonance phenomenon called 'lock-in' occurs. This lock-in causes intensification of the vibrations and noise level [8, 11].

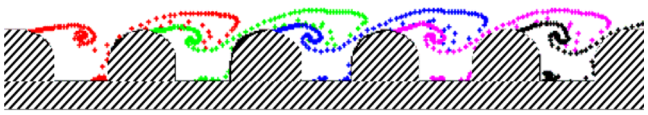

Figure 1.4: Shedding of vortices over a simplified carcass geometry [5].

It was observed that a high moisture content in the gas flow tends to reduce this noise [5]. This led Belfroid et al. [12] to perform experiments in corrugated pipes in singing conditions with liquid injection, as shown in Figure 1.5. The experiments showed that liquid volume fractions as low as 0.03% were sufficient to eliminate whistling. The following three mechanisms were proposed as possible reasons for this mitigation:

- Fill-up of corrugations by the injected liquid, which reduces the source strength as the cavity depth decreases.
- Increase in damping due to the presence of droplets in the flow and liquid on the wall.
- Decrease in source strength due to an increase in the boundary layer thickness as a consequence of droplets, rivulets or film on the walls, which act as additional roughness.

Many attempts have been made earlier by researchers to study the dominant mechanism leading to whislting mitigation, but they have all largely been unsuccessful [12–14]. The individual contribution of each mechanism has not been quantified and it is believed that all the mechanisms play a role in the attenuation of sound. However, van Eckeveld et al. [15] have recently shown that the filling of the corrugations is strongly correlated to the reduction in sound amplitude. The altered cavity geometry due the liquid fill-up was proposed as the main cause of this reduction.

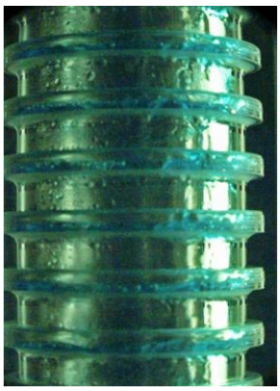

Figure 1.5: Snapshot of the presence of liquid in a corrugated pipe with air-water flow [12].

1.3. Research Objective

Since the first mechanism proposed by Belfroid et al. [12] seems to have a dominant effect on the whistling mitigation, the characteristics of the cavity fill-up is studied in more detail. The effect of varying flow parameters on the cavity filling behaviour are still unknown. The objective of this thesis therefore is framed as:

To study the cavity filling behaviour, such as the amount of filling and the geometrical changes of the cavity structure, due to a liquid film driven by a gas flow at varying gas-liquid flow rates.

It should be noted that this thesis is only concerned with the two-phase flow aspects and acoustical aspects are not studied. A dedicated experimental setup is constructed which creates a vertically upward air-water flow in a rectangular channel. Water is injected as a film on one side of the channel which has a cavity manufactured on it. Experiments are performed to measure the thickness of the liquid film entering the cavity. The liquid filling inside the cavity is then quantified and related to the incoming film thickness.

1.4. Outline of the Thesis

The aim of this thesis is to analyze the cavity filling behaviour due to the liquid film driven by a gas flow. The important theory relevant to the problem and previous research done on cavity sound mitigation are presented in Chapter 2. The experimental setup and the different measurement and flow visualization techniques used in the current work are explained in Chapter 3. The results obtained are then presented and discussed in Chapter 4. Lastly, the insights obtained from this work are presented as conclusions and the recommendations for further research are given in Chapter 5.

2

Theoretical Background

In this section, the relevant theory and literature review are presented. First, the basic concepts of fluid dynamics including the governing equations, the relevant non-dimensional numbers and a description of shear flows are presented. Later, different types of cavity flows are introduced and the self-sustained oscillation phenomenon that leads to the sound generation in cavities is explained. Lastly, the different sound mitigation methods are presented with particular emphasis on the liquid injection method.

2.1. Governing Equations

Fluid dynamics is governed by the laws of conservation of mass, momentum and energy. The first equation stating the mass conservation, is called the continuity equation and is given as [16]:

$$\frac{D\rho}{Dt} + \rho(\vec{\nabla} \cdot \vec{u}) = 0, \tag{2.1}$$

where ρ is the fluid density and $\vec{u}$ is the fluid velocity vector. When the fluid flow is such that the ratio of its speed to the speed of sound in that medium is less than 0.3, the changes in fluid density are negligible and the fluid is called incompressible (see mach number, Section 2.2). The first term from Equation 2.1 drops out and the equation simplifies to:

$$\vec{\nabla} \cdot \vec{u} = 0 \tag{2.2}$$

The second equation governs the conservation of momentum. For a Newtonian, incompressible fluid, the equation takes the following form [16]:

$$\rho\frac{D\vec{u}}{Dt} = -\vec{\nabla}p + \mu\vec{\nabla}^2\vec{u} + \sum f_{body}, \tag{2.3}$$

where p is the pressure, μ the viscosity of the fluid and f_{body} are the external body forces experienced by the fluid. The third equation is the conservation of energy, which is neglected in this case since the changes in temperature and density are negligible and the flow is considered incompressible.

2.2. Non-dimensional Numbers

Non-dimensional numbers are important in fluid mechanics, as they give the relative importance of the different terms of a governing equation. They also help to reduce the number of variables and therefore reduces the number of experimental runs. There exists two main methods of obtaining the relevant non-dimensional numbers. One is using dimensional analysis, where all the important variables such as the physical properties, geometry and flow variables are chosen and the exponents of the variables are determined that make the parameter non-dimensional. Another approach is the non-dimensionalization of the equation governing the physics of the system. The non-dimensional numbers relevant to this work are described in this section.

- Mach Number (Ma): Mach number is the ratio of the flow velocity to the speed of sound in the flowing medium.

$$Ma = \frac{\text{Flow velocity}}{\text{Speed of sound}} = \frac{U}{c}, \tag{2.4}$$

  where U is the flow velocity and c is the speed of sound. Mach number is used to determine compressibility effects in a fluid. When $Ma < 0.3$, the fluid can be considered as incompressible, as its density does not change considerably. In this study, Ma is in the order $\mathcal{O}(10^{-2})$, with a bulk gas velocity range of $25 - 30\ m/s$ and taking the speed of sound as $343\ m/s$ at $20°C$.

- Reynolds number (Re): The Reynolds number is one of the most important non-dimensional number in fluid dynamics. It gives the relative importance of the inertial and viscous forces in the flow and is defined as:

$$Re = \frac{\text{Inertial forces}}{\text{Viscous forces}} = \frac{\rho U L}{\mu}, \tag{2.5}$$

  where U and L are the characteristic velocity and length scale respectively, ρ is the fluid density and μ is the fluid viscosity. In the current work, Reynolds number is only used for the gas phase and the bulk gas velocity (U_g) is used as the characteristic velocity. The length scale used is denoted as a subscript. At low Reynolds number ($Re < 2300$), a laminar flow occurs and the viscous forces dominate over the inertial forces. When the Re is high ($Re > 4000$), the flow transitions to a turbulent regime. Unlike laminar flow, turbulent flows are irregular and chaotic in nature and are characterised by formation of eddies, leading to lateral mixing.

- Weber number (We): Weber number is a measure of the relative importance of the disruptive inertial forces and the stabilizing interfacial (surface tension) forces. It is given by the ratio:

$$We = \frac{\text{Inertial forces}}{\text{Surface tension forces}} = \frac{\rho U^2 L}{\sigma}, \tag{2.6}$$

  where σ is the surface tension. Weber number is useful in analysing multiphase flows, such as the formation of bubbles and droplets. In our case of two-phase flow through a cavity, We is important as inside the cavity, there is a competition between the inertial forces which tends to shear away the liquid and the surface tension forces, which tries to hold the liquid inside the cavities.

2.3. Boundary Layers

As has been already introduced in Section 1.2, one of the main causes of sound production when gas flows over the cavities of a corrugated pipe is the formation of a shear layer over the cavities. The detailed description of this mechanism is given later in this chapter. But before diving into it, a general understanding of shear flows is necessary to understand the FIP in flexible risers. Shear layers are formed by virtue of the viscosity of a fluid, when a free flowing stream with a velocity U_∞ comes in contact with a solid or fluid boundary moving at a different velocity. Initially, a velocity discontinuity is formed due to this difference in velocity. However, due to the viscosity of the fluid, the velocity discontinuity smooths out and a velocity gradient is created over some distance. This discontinuity extends from somewhere in the free stream area to the solid surface or up to the free stream area of the other fluid if the interaction is between two fluids. Therefore, the flow is divided into two regions: a shear flow region where viscosity effects are significant and the core region where the flow can be considered inviscid. In case of the boundary being a solid surface, this region is called a boundary layer, whereas for a fluid boundary, it is called a mixing layer. The boundary layer will be considered first, followed by an explanation of the mixing layer.

Considering a stationary wall, when the free flowing fluid interacts with it, as shown in Figure 2.1, a no-slip condition is imposed on the fluid. This condition requires the velocity of the fluid in direct contact with the wall to be zero. Viscous shear stresses develop on this stationary layer and the layer on top of it and the top layer decelerates. In a similar fashion, the fluid deceleration gets transferred successively to the next layers upto a distance δ where the velocity of the layer matches the free stream velocity. The distance δ is called the boundary layer thickness.

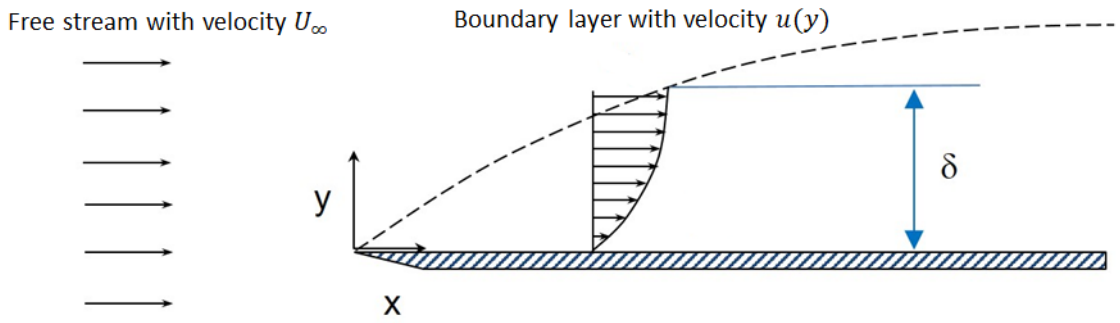

Figure 2.1: The development of boundary layer on a flat plate. The boundary layer thickness is denoted as δ. (Adapted from wikipedia.org).

The boundary layer thickness and the velocity profile in the layer depends on the flow conditions. For a flat plate, the boundary layer is initially laminar. The exact solution for the development of a laminar boundary layer on a flat plate exists and is called the Blasius solution. The laminar boundary layer thickness grows with distance and after a critical Re_x (in the range of 10^5 to 10^6 [17]), based on the streamwise distance on the plate x, the boundary layer transitions to turbulent. Unlike laminar boundary layers, no exact solution is available for turbulent boundary layers, however, empirical solutions exists.

The mean velocity profile for turbulent flows are often approximated as a power-law as given in Equation 2.7 [18].

$$\frac{u(y)}{U_\infty} = \left(\frac{y}{\delta}\right)^{\frac{1}{n}}, \tag{2.7}$$

where n is called the shape factor. The value of n is generally taken as 7 for a fully-developed pipe flow and consequently Equation 2.7 is called the one-seventh power-law.

There are three commonly used methods to quantify the boundary layer thickness:

- 99 % boundary layer thickness (δ_{99}): This thickness is defined as the height where the velocity in the boundary layer reaches 99% of the free stream velocity U_∞. That is $u = 0.99U_\infty$. The laminar and turbulent δ_{99} are given in Equations 2.8 and 2.9 [17].

$$\frac{\delta_{99}}{x} = \frac{5}{Re_x^{1/2}} \tag{2.8}$$

$$\frac{\delta_{99}}{x} = \frac{0.16}{Re_x^{1/7}}, \text{ for n = 7} \tag{2.9}$$

- Displacement thickness (δ_*): The displacement thickness is defined as the distance through which the surface needs to be moved, for a hypothetical inviscid flow to have the same mass flux as the real fluid. Balancing both the mass fluxes gives the mathematical description of the displacement thickness as:

$$\delta_* = \int_0^\infty \left(1 - \frac{u}{U_\infty}\right) dy \tag{2.10}$$

For laminar and turbulent regimes respectively, the equations are [16]:

$$\frac{\delta_*}{x} = \frac{1.72}{Re_x^{1/2}} \tag{2.11}$$

$$\frac{\delta_*}{x} = \frac{0.020}{Re_x^{1/7}}, \text{ for n = 7} \tag{2.12}$$

- Momentum thickness (θ): Similar to the displacement thickness, θ is the height the surface needs to be moved to balance the momentum difference in a real and inviscid flow. A momentum balance results in:

$$\theta = \int_0^\infty \frac{u}{U_\infty}\left(1 - \frac{u}{U_\infty}\right) dy \tag{2.13}$$

The laminar and turbulent momentum thickness are given respectively as [16]:

$$\frac{\theta}{x} = \frac{0.664}{Re_x^{1/2}} \tag{2.14}$$

$$\frac{\theta}{x} = \frac{7}{72}\delta_{99}, \text{ for n = 7} \tag{2.15}$$

2.4. Mixing Layers

A mixing or shear layer is formed when a fluid stream comes in contact with another nearly parallel fluid stream with a different velocity. Such a mixing layer, when two streams with velocities U_h and U_l such that $U_h > U_l \geq 0$ interact with each other is shown in Figure 2.2. For a mixing layer, two characteristic velocities can be defined: the convective velocity (U_c) which is the average of the stream velocities (Equation 2.16) and the velocity difference (U_s) which is the difference in the velocities of the fluid streams (Equation 2.17).

$$U_c = \frac{1}{2}(U_h + U_l) \tag{2.16}$$

$$U_s = U_h - U_l \tag{2.17}$$

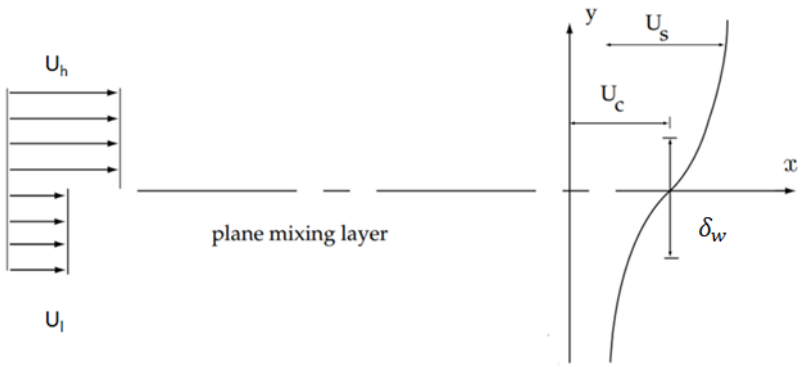

Figure 2.2: A plane mixing layer with two fluid streams having velocities U_h and U_l. The width of the mixing layer is denoted by δ_w, the convective velocity by U_c and the velocity difference by U_s. Adapted from [18].

.

Similar to the boundary layers, when the two fluid streams come in contact, a sharp velocity discontinuity is formed. As the downstream distance increases, the effect of viscosity comes into play which smooths out the sharp discontinuity. As a result, the width of the mixing layer increases. The mixing layer width is generally expressed in terms of the local vorticity thickness ($\delta_w(x)$) as given in Equation 2.18 [19].

$$\delta_w(x) = \frac{U_s}{\frac{dU}{dy}_{\max}}, \tag{2.18}$$

where $dU/dy_{\max}$ is the maximum gradient in the mean velocity. The inflexion point in the mean velocity profile means that it is inviscidly unstable and velocity perturbations can be amplified due to the Kelvin-Helmholtz instability mechanism. Wave like disturbances are created, which are convected downstream with velocity U_c. The disturbances grow as they move downstream and non-linear effects come into play due to which the vortices roll-up.

2.5. Cavity Flows

Cavity flows have long been a subject of research both from the fundamental and practical point of view. A large number of studies has been done especially in the area of flow induced noise, generated

by flow over weapon bays in aircrafts, open car sunroofs and corrugated tubes. Since gas flow over flexible risers can be a source of sound, it is important to have an overview of the characteristics of flow over different cavity geometries. Two-dimensional cavities are classified based on their length (L_c) and depth (D_c), which is shown in Figure 2.3 and described as follows [20, 21]:

- Deep: Cavities with a length to depth ratio (L_c/D_c) < 1.
- Shallow: These have a L_c/D_c ≥1. Further, they are divided based on the range of L_c/D_c ratios.
  - Open: The L_c/D_c ranges from 1 to 9. In this regime, shear layer is formed at the upstream cavity edge, which spans the length of the cavity and impinges on the downstream cavity edge. The cavity is occupied by one large recirculation region at the center which is isolated from the main flow and with smaller recirculation zones at the upstream and downstream wall bottom.
  - Closed: Long cavities with L_c/D_c > 12 fall into this category. The shear layer that separates from the upstream corner reattaches to the cavity bottom, then detaches again before the downstream wall, thus forming two recirculation regions.
  - Transitional: L_c/D_c extends from 9 to 12. It shows characteristics of both the open and closed type cavities.

The cavities can be further classified when accounting for its width (W_c) as:

- Wide: Cavities which are wider than they are long (L_c/W_c < 1) fall into this category. Flow over wide cavities is essentially two-dimensional, with coherent shear layer vortices spanning across the width.
- Narrow: They have a L_c/W_c > 1. The side walls makes the flow highly three-dimensional.

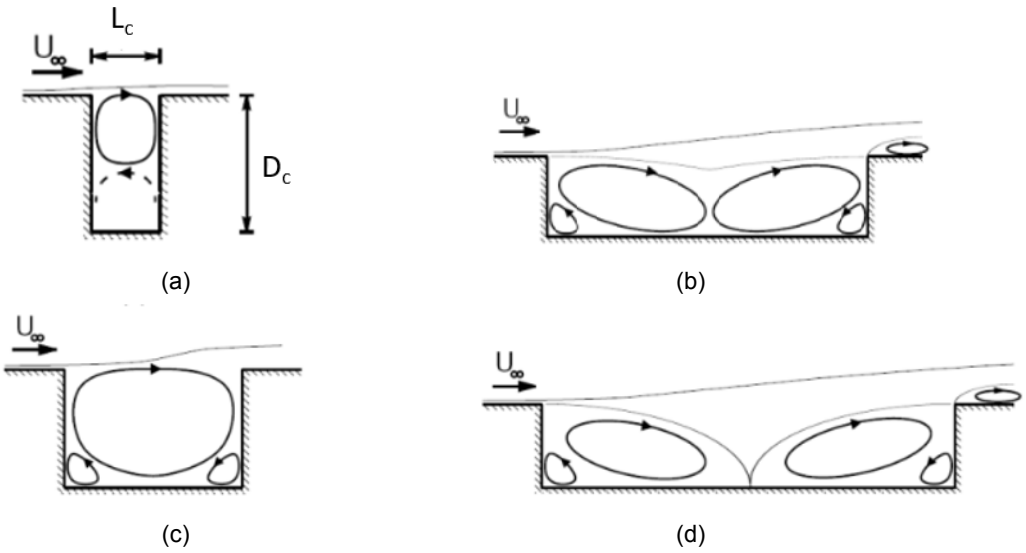

Figure 2.3: Different cavity geometries. (a) Deep, (b) transitional, (c) shallow - open, (d) closed. Adapted from [21].

Typical riser corrugations have dimensions such that the they are shallow open. Therefore, the cavity used in this thesis is also chosen to be of the shallow open geometry (see Section 3.2 of Chapter 3). Also, a wide cavity is chosen so as to obtain a two-dimensional shear layer over the cavity.

2.5.1. Cavity Modes

When a fluid flows over a cavity, the main flow detaches from the cavity upstream edge and forms a shear layer with the quiescent flow in the cavity. Gharib and Roshko [22] suggest there is a particular 'mode' selection which determines the flow regime that occurs for flow over cavities. The different modes are classified based on the ratio of the cavity length to the momentum thickness of the boundary layer upstream of the cavity $\left(\frac{L_c}{\theta}\right)$ and are called as the non-oscillating, shear layer and wake modes. The flow characteristics of these modes are shown in Figure 2.4 and described as follows:

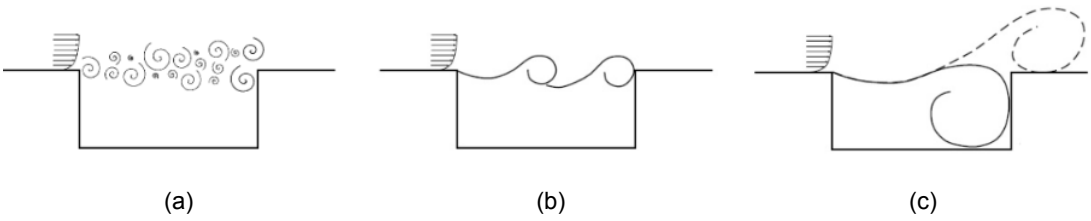

Figure 2.4: Cavity flow modes: (a) non-oscillating, (b) shear layer mode and (c) wake mode. Adapted from [23].

- Non-oscillating mode: When the ratio $\frac{L_c}{\theta}$ < 80, small vortical structures are formed. The vortical structures do not organize into periodical vortices and impinge on the downstream corner randomly which is heard as white noise.
- Shear layer mode: This mode is observed when 80 < $\frac{L_c}{\theta}$ < 120. It is characterized by the self-sustained oscillations of large scale coherent vortices generated in the shear layer.
- Wake mode: When $\frac{L_c}{\theta}$ > 120, the flow field resembles that of a bluff-body wake, which gives it its name [22]. This mode is characterized by vortical structures comparable in size to the cavity depth. Unlike the shear layer mode, the vortices reattach to the bottom of the downstream edge and ejects out of it. Thus there is a large interaction between the internal cavity flow and free stream flow. Interestingly, the wake mode has been observed mostly in two-dimensional numerical simulations [24, 25]. Suponitsky et al. [25] observed that the flow regime transitioned from wake mode to the shear layer mode, when a three-dimensional perturbation was added to the flow.

2.5.2. Self-sustained Oscillations

As was mentioned earlier, self sustained, periodically oscillating shear layers impinging on the downstream corner of the cavity are a source of sound. The feedback mechanism leading to this self sustained oscillation in the shear layer is discussed here.

The shear layer that is formed at the upstream cavity edge grows as it is convected to the downstream edge and three regions can be distinguished with a piecewise linear growth rate as shown in

Figure 2.5 [21]. A high growth rate is observed in the first region due to the formation of large scale Kelvin-Helmholtz vortices. This growth occurs due to a collective interaction of numerous small vortices shed at the instability frequency. The second region is characterized by growth due to viscous spreading and entrainment of the surrounding fluid. In the third region, the impingement process at the downstream edge influences the shear layer growth. A vertical velocity component is generated due to the inflow-outflow motion near the downstream corner leading to a high growth rate.

After the impingement, part of the shear layer is diverted into the cavity region as a wall jet-like flow along the vertical wall of the downstream edge. This is a source of disturbance due to the vorticity embedded in it from the boundary layers formed at the cavity walls. The upstream propagation of these disturbances acts as a feedback to the shear layer, which can be of two types: fluid-dynamic or acoustic. For incompressible flows, the feedback is essentially fluid-dynamic, whereas for compressible flows resonant wave effects become important and acoustic feedback dominates. In the present work, the gas flow velocities are such that $Ma < 0.3$ and therefore the flow can be considered incompressible. Hence fluid-dynamic feedback would be the acting mechanism. The feedback of the disturbances induces localized vorticity fluctuations at the shear layer near the separation. These vorticity fluctuations are then amplified along the cavity length, which finally impinge on the downstream corner again to close to feedback loop. An overview of the feedback mechanism is shown in Figure 2.6.

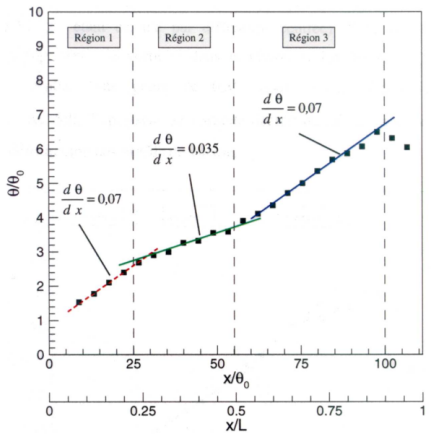

Figure 2.5: Mixing growth rate over a cavity with $L_c/D_c = 0.42$, $Ma = 0.8$, $Re_L = 8.6 \times 10^5$ [21].

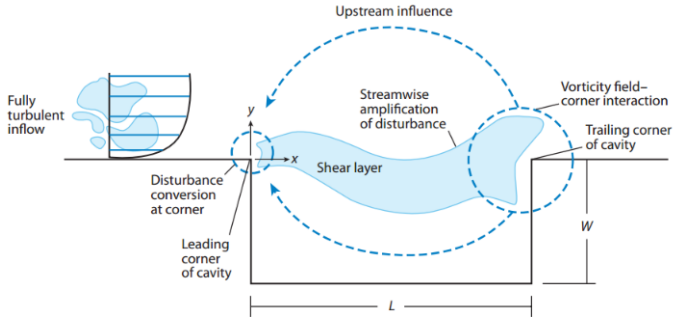

Figure 2.6: Feedback mechanism for a cavity flow [26].

The impingement of these vortical structures at the downstream edge causes pressure pulsations which can be percieved as sound (Figure 2.7). The frequency with which the impingement occurs is given as [21]:

$$f = (n + \frac{1}{4})\frac{U_c}{L_c} \tag{2.19}$$

Or in terms of Strouhal number,

$$St = \frac{fL_c}{U_\infty} = (n + \frac{1}{4})\frac{U_c}{U_\infty}, \tag{2.20}$$

where n is the mode of oscillation, U_∞ is the free stream velocity, U_c is the convective velocity of the vortices in the shear layer and L_c is the cavity length. When this frequency matches with one of the natural frequencies of the corrugated pipe, a 'lock-in' occurs which can cause the acoustic oscillations

of the pipe to be resonantly excited [7]. With an increase in the flow velocity, the frequency increases in steps, corresponding to the mode (n) of oscillation, as shown in Figure 2.8. This also leads to a constant Strouhal number, which lies in the range of 0.32-0.5 for typical corrugated pipes [27].

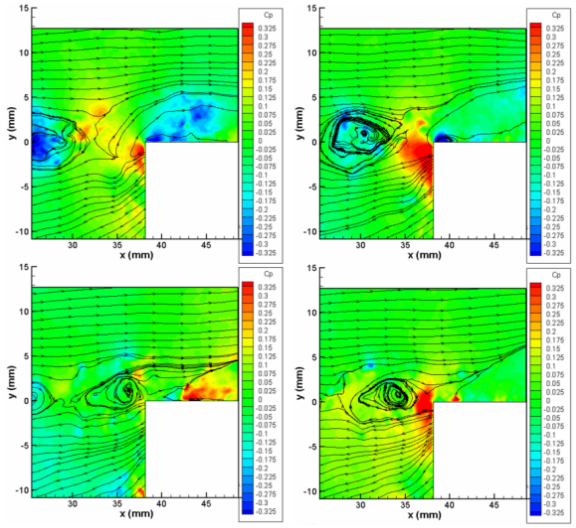

Figure 2.7: Pressure fluctuations at the downstream corner caused by vortex impingement. Time progresses clockwise [28].

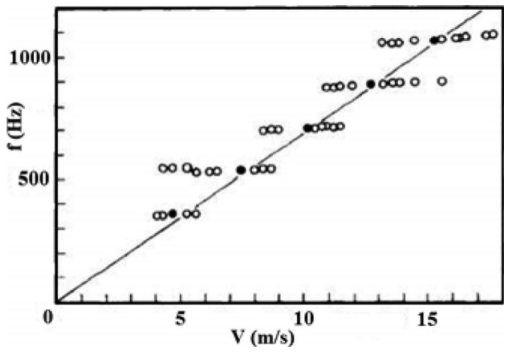

Figure 2.8: Step-wise jumps in frequency with increase in free stream velocity [8].

2.6. Mitigation Methods

Because of the detrimental effects of self sustained oscillations on the corrugated pipe structure, a lot of previous literature is available on its whistling mitigation. However, most of these studies are concerned with the alteration of the cavity structure itself (Figure 2.9). Petrie and Huntley [29] observed a decrease in the sound pressure levels when some wrinkles were introduced close to the corrugations, as shown in Figure 2.9a. They suspected that this was due to the change in turbulence structures close to the wall, which changes the vortex shedding process. However, it could not be proven due to difficulty in measuring near the wall. They also observed that adding a smooth pipe section upstream of corrugated pipe leads to reduced sound pressure levels. A similar observation was made by Shetler and Bryson [30], and Romero [31], but instead of wrinkles on the cavity bottom, they roughened the plateau region. Other control methods include adding ramps, spoilers and vortex generators to the cavity, as shown in Figure 2.9b [32–34].

These passive control methods are not feasible for the flexible risers case, since the carcass is made by interlocking steel ribbons and geometric alteration could be a complex task and could affect the structural integrity of the riser as well. Furthermore, a solution is needed that could be applied to existing riser systems.

Belfroid et al. [6] observed that injecting small amounts of liquid eliminated the singing in corrugated pipes. Comprehensive experiments were done in vertical and horizontal corrugated pipes of $49\ mm$ internal diameter with air-water flow. They observed that increasing liquid flow rates results in the

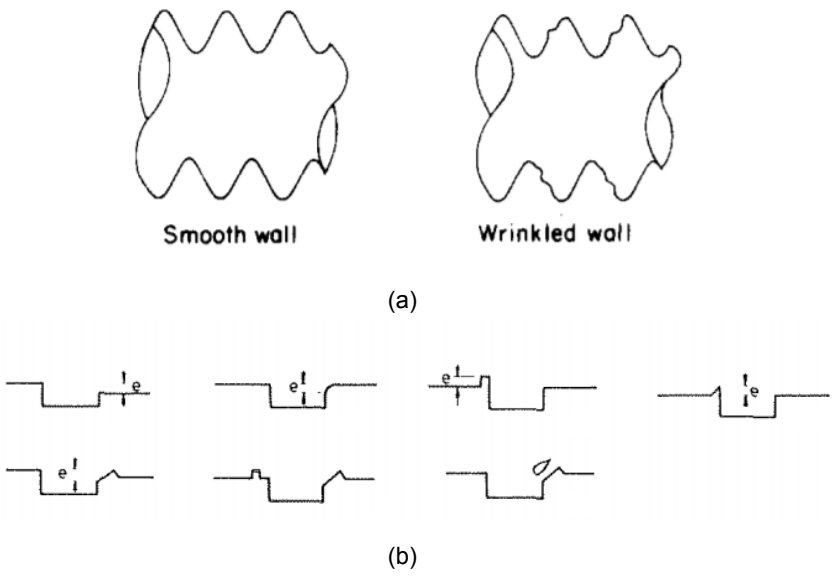

Figure 2.9: (a) Addition of wrinkles on the corrugated structure by Petrie and Huntley [29], (b) different geometrical variations on the cavity structure to attenuate sound [34].

increase of gas onset velocity for whistling, as shown in Figure 2.10a for a horizontally inclined pipe. At a particular gas velocity, the pressure amplitude decreased almost linearly with increasing liquid flow rates for both the horizontal and vertical cases. However, liquid in the vertical case seemed to be more effective in amplitude reduction (Figure 2.10b). The reason for this can be understood from the flow visualization in both the cases, as shown in Figure 2.11. In the horizontal case, a stratified film is present at the bottom of the pipe with liquid creep-up inside the cavities, whereas for the vertical flow, liquid is present across the perimeter of the cavities making it more effective in amplitude mitigation.

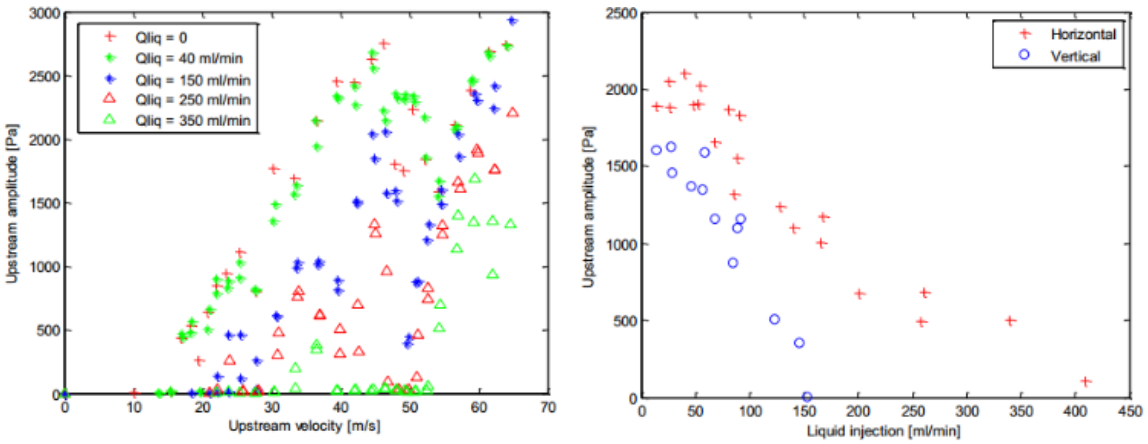

Figure 2.10: (a) Increase in onset velocity with liquid injection for the horizontally aligned corrugated pipe, (b) amplitude reduction with liquid injection rate for the vertical and horizontal configurations at a particular gas velocity [12].

Three main mechanisms were proposed as plausible reasons for the observed sound mitigation by liquid injection:

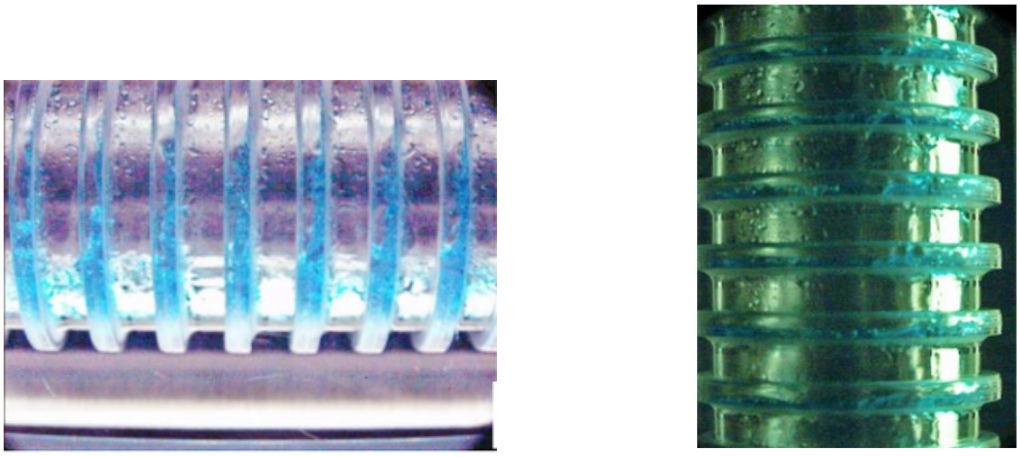

(a) (b)

Figure 2.11: Snapshots from high speed recordings showing presence of liquid in the corrugations for (a) horizontal, and (b) vertical corrugated pipes [12].

- Source strength reduction due to fill-up of corrugations: Nakiboğlu et al. [35] have shown that the acoustic source strength of a corrugation is dependent on the cavity depth. Liquid inside the corrugations acts like a modulated bottom contour [36]. Therefore, it leads to a decrease in the effective depth of the cavities and the associated source strength. van Eckeveld et al. [15] have also shown that there is a strong correlation between the fraction of corrugations filled with liquid and the reduction in whistling.

- Increase in damping: Droplets present in the flow and liquid film present at the plateaus of the corrugated pipe increases the acoustic damping coefficient. Golliard et al. [14] tried to quantify the acoustic damping in horizontal smooth and corrugated pipes due to the presence of droplets. A linear increase in the damping coefficient with liquid injection rate was measured in the case of a smooth pipe. For the corrugated pipe, instead of an increase in damping coefficient, a decrease in the negative damping coefficient (indicating a reduced source strength) was observed near the source frequency.

  It was suspected that liquid on the walls or inside the cavities caused this. Hence, the isolated effect of damping due to droplets could not be studied and it was concluded that damping could occur due to a combination of mechanisms.

- Additional source strength reduction: The presence of droplets, rivulets or liquid film on the cavity plateaus act as additional roughness for the gas flow. This leads to a thicker boundary layer and as a result a thicker and more stable shear layer over the cavity [37]. Hence the L_c/θ ratio decreases and self-sustained oscillations are suppressed. Furthermore, liquid on the wall can be transported to the shear layer in the form of droplets and affect the shear layer instability. Sanna et al. [13] studied the contribution of liquid film to the sound mitigation in upward oriented 1 inch side branches (it has been shown that the side branches have similar acoustic behaviour as corrugated pipes [27]). They found a 60% reduction in pressure amplitude above the flow

rates at which the water was convected with the shear layer (at lower rates liquid bypasses the side branch, see Figure 2.12). They concluded that the reduction in amplitude is dependent on the local liquid flow pattern.

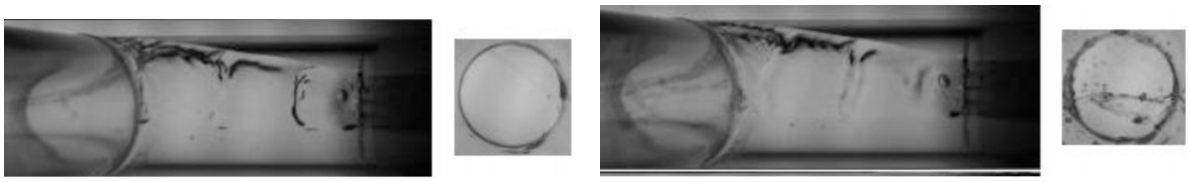

(a) (b)

Figure 2.12: Side and top view of the side branch with liquid injection rates such that (a) there is no interaction between liquid and shear layer, (b) liquid is convected with the shear layer [13].

2.6.1. Relative Importance of the Mechanisms

A lot of attempts have been made to quantify the individual contribution of the various mechanisms. As mentioned in the previous paragraph, the attempt of Golliard et al. [14] to isolate the damping due to the presence of droplets in corrugated pipe was unsuccessful. Belfroid et al. [12] calculated the required damping to achieve the measured amplitudes as a function to liquid rate, assuming a constant source. But the required damping was found to be almost 10 times higher than the expected damping, calculated by assuming the presence of $100\ \mu m$ droplets. In the experiments of Sanna et al. [13], measurements were done on three different configurations based on the position of the liquid injector with respect to the side branch opening. Although a steep decrease in pressure amplitude was measured for one of the configurations when the liquid interfered with the shear layer, the reduction in amplitudes for the other two configurations were not significantly different. The common feature in all the three configurations was the accumulation of liquid at the wall between the two side branches, which they suspect causes additional acoustic damping. All of these studies show that a combination of all of these mechanisms are involved in the whistling mitigation. The relative importance of each mechanism would depend on the flow regime in the corrugated pipe, leading to either a reduction in source strength or an increase in damping. A recent work by van Eckeveld et al. [15] showed that the the amount of filling in the cavities was directly correlated to the reduction in whistling amplitude, as shown in Figure 2.13. They noted that for all gas flow rates, the whistling stopped completely after a particular filling threshold. An altered cavity geometry, such as a reduced cavity length or a changed upstream cavity edge from where the flow separation takes place was suggested as the reason for the reduction in whistling amplitude. The changed geometry can possibly lead to a reduced value of L_c/θ such that the whistling does not occur. This led the authors to manufacture a corrugated pipe with cavity geometry matching the liquid filled cavity at no whistling case. This corrugated pipe did not whistle when passing gas flow without any liquid injection, hence confirming their hypothesis.

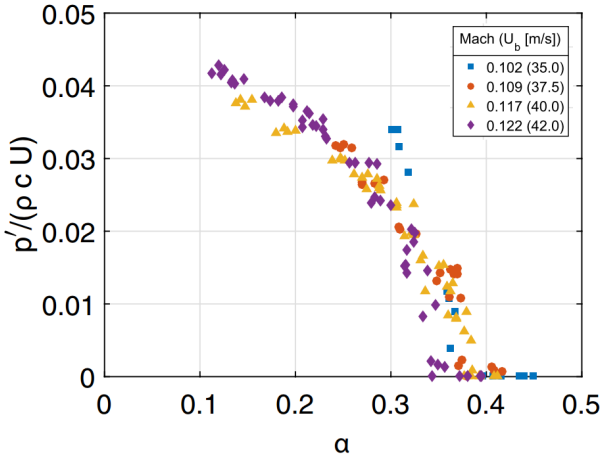

Figure 2.13: The dimensionless whistling amplitude plotted with respect to the cavity filling ratio α [38]. A higher filling ratio causes more reduction in the whistling amplitude, upto a critical filling ($\alpha \approx 0.4$) after which the whislting is completely suppressed.

3

Experimental Setup and Techniques

In this chapter the details of the experiments conducted in the framework of this thesis are described. First, the requirements that the experimental setup needs to fulfil, in order to study the interaction of the two-phase flow with the cavity are described. This is followed by the details of the experimental setup used for this study. Finally, a brief overview of the different measurement techniques used in this work is given.

3.1. Setup Requirements

The experimental setup is required to create a liquid film on a surface which is dragged up by gas flow. The surface on which the film is created should also include a cavity, which allows us to study the interaction of flow with it. The requirements are imposed based on literature study of the relevant dimensionless parameters, while considering the practical feasibility due to material availability, costs and space requirement. These requirements are described below.

Gas Flow

A continuous vertically upward flow of air is required to flow through the setup. In order to obtain a cavity Reynolds number (Re_{L_c}) in the same range as in the literature, air flow speeds (U_g) in the range of 25 to $30\ m/s$ are chosen, based on a cavity length of $L_c = 10\ mm$ [12, 15, 36]. This results in Re_{L_c} range of 1.6×10^4 to 1.98×10^4. The lower limit of air speed is restricted due to the inability of the air flow to support the upward liquid flow, as below this limit, liquid starts to fall down. The upper limit of the air flow speed is restricted, as the additional pressure drop generated due to the liquid injection cannot be overcome by the fan used to create the air flow.

Liquid Flow

Water is selected as the working liquid, which flows cocurrently with the gas flow. An initial estimate of the required flow rate is made by a simple perimeter scaling from the experiments of Belfroid et al.

[12]. The authors used a liquid flow rate of up to $350\ mL/min$ in a $49\ mm$ internal diameter corrugated tube, which is scaled according to $Q_l = Q_l' \frac{P}{P'}$ (see Figure 3.1). Here, P' & Q_l' are the perimeter and flow rate in the experiments of Belfroid et al. [12] and P & Q_l are the same parameters relevant to the current work where a rectangular channel is used. This scaling results in a required liquid flow rate of $1.5\ L/min$. Flow rate is therefore varied between 0.5 to $2.8\ L/min$, resulting in a liquid volume fraction in the range of $2.4 \times 10^{-5} \leq \phi_l \leq 1.7 \times 10^{-4}$, which is comparable to the works of Belfroid et al. [12] and van Eckeveld et al. [15]. Liquid volume fraction is defined as the ratio of the liquid volume flow rate to the total (gas+liquid) volume flow rate, that is:

$$\phi_l = \frac{Q_l}{Q_g + Q_l}\ , \tag{3.1}$$

where Q_l is the volume flow rate of liquid and Q_g is of the gas.

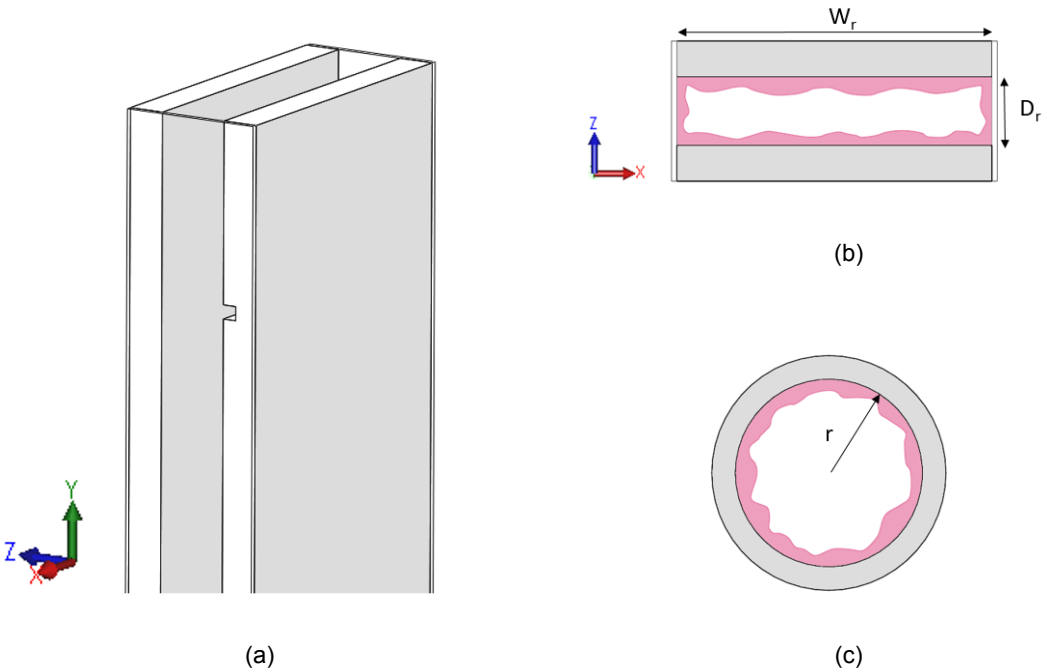

Figure 3.1: (a) Representation of the rectangular channel used in this work. (b) Topview of the rectangular channel with area $A = W_r \times D_r$, perimeter $P = 2(W_r + D_r)$ and with liquid flow rate Q_l, (c) the tube used by Belfroid et al. [12] with perimeter $P' = 2\pi r$ and liquid flow rate Q_l'.

Test Section

The air-water mixture is required to flow through a test section containing a cavity to study its filling. A rectangular channel with a cavity positioned at the same side as the liquid injection is therefore required. The channel should be wide enough such that the ratio of the cavity length to the channel width is small $(L_c/W_r << 1)$. In that case, the side walls do not induce strong three-dimensional effects in the shear layer over the cavity [21].

The distance between the two opposite plates (D_r) should be kept such that the confinement ratio lies in the range of $2 \leq (D_r/L_c) \leq 30$, which is generally found in corrugated risers. Furthermore,

sufficient development length should be available for the gas flow to be fully-developed at the entrance of the cavity. This development length is a function of the channel Reynolds number (Re_{D_h}) and is given as $L/D_h = 4.4Re_{D_h}^{1/6}$ [39], where $D_h = \frac{4\times A}{P}$ is the equivalent or hydraulic diameter. A and P are the area and perimeter of the channel respectively, defined in Figure 3.1b. In practical engineering applications, the development length is often approximated as $L = 10D_h$, as the entrance effects are insignificant after this length [39]. Due to space contraints, this approximation is used in the present study. The channel should be enclosed and leak-proof and made of a transparent material so as to provide optical access for the measurements.

3.2. Construction

The experimental setup is schematically depicted in Figure 3.2. It consists of the wind tunnel, which supplies gas flow to the test section (components A, B and C) and the liquid injection system to create a liquid film inside the channel (E to I, alphabetically). The gas-liquid mixture is then discharged out from the top into a hose (J) from where gas is released into the atmosphere and liquid is collected in a reservoir (K).

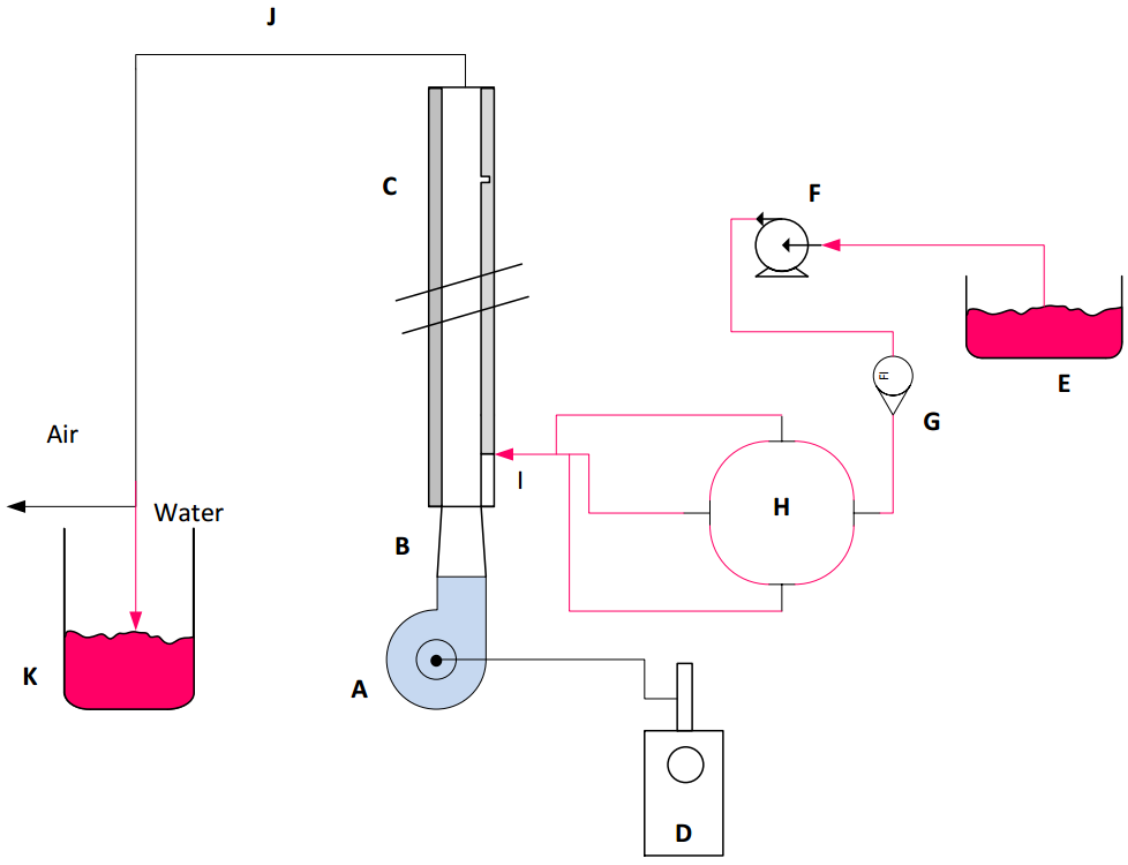

Figure 3.2: Schematic diagram of the experimental setup, (A) centrifugal fan with pitot at the inlet, (B) contraction, (C) rectangular channel with cavity, (D) Betz manometer, (E) reservoir containing dyed water, (F) water pump, (G) rotameter, (H) tube loop, (I) liquid injection box with three injection ports, (J) air-water mixture from channel exit, (K) water collection reservoir.

3.2.1. Wind Tunnel

A wind tunnel is a device that produces a continuous stream of air to study the interaction of flow with the models being tested. Wind tunnels can be classified on the basis of their construction layout as closed circuit or open circuit. In a closed circuit wind tunnel, air that passes through the test section is recirculated by the fan. This air recirculation leads to low power requirements for the fan, but at the expense of increased construction costs. On the other hand, open circuit wind tunnels discharge the air after it passes through the test section to the atmosphere. Fresh air needs to be drawn continuously, resulting in higher fan power requirements compared to closed circuit tunnels. The advantages of using an open circuit tunnel are its lower construction costs and lower space requirements [40]. An open circuit tunnel is chosen for this study because a two-phase flow of air and water is required, which might damage the driving unit if a closed circuit tunnel is used. The constructed wind tunnel includes a driving unit, rectangular channel with cavity and a contraction connecting the driving unit to the rectangular channel.

Driving Unit

A driving unit creates the required air flow in the channel. The driving unit can either be an axial or centrifugal fan. However, a centrifugal fan is recommended as it provides a steadier and more efficient operation over a wide range of operating conditions as compared to an axial fan [40]. A *Dietz DN 18* centrifugal fan is therefore used.

The fan speed is varied by using a frequency converter. To have a reproducible air flow, the inlet velocity of the fan is measured with a pitot tube. A pitot tube is a device which measures the dynamic pressure of the flow, from which the flow velocity can be obtained (see Section 3.3). This dynamic pressure is obtained from a Betz manometer to which the pitot tube is connected. A constant air flow rate entering the fan can therefore be ensured by keeping the inlet velocity constant. The position of the pitot tube in the inlet plane is not critical because the flow entering the fan should be uniform. It is therefore positioned at the center of the fan inlet, as shown in the Figure 3.3. The alignment of the pitot tube with the flow, however, is important and misalignment could induce errors in the measured velocity. It is therefore carefully positioned so as to be aligned with the axis of the fan inlet.

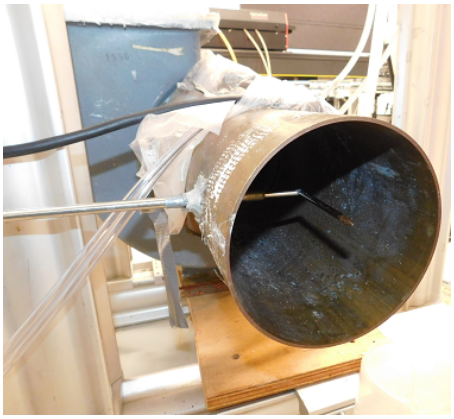

Figure 3.3: Pitot tube at the inlet of the centrifugal fan.

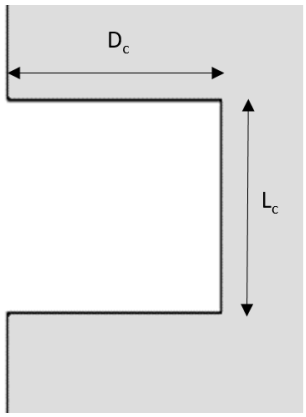

Figure 3.4: The cavity geometry used in the experiments. The cavity has a length (L_c) and depth (D_c) of $10\ mm$.

Rectangular Channel

The rectangular channel containing a cavity is constructed through which air and water flows. The cavity is square shaped and has a length (L_c) and depth (D_c) of $10\ mm$, as shown in Figure 3.4. Therefore, the cavity falls in the shallow open classification. The rectangular channel has a width (W_r) of $230\ mm$ and the cavity spans across the entire width. The distance between the two plates (D_r) is $50\ mm$, resulting in a confinement ratio (D_r/L_c) of 5. The total length of the channel is $1.5\ m$ and the cavity is positioned at a distance of $1.2\ m$ from the bottom of the channel. The hydraulic diameter of the channel (D_h) is $82\ mm$. This results in the development length for the cavity to be $14.5D_h$. Since this length is larger than the required development length $10D_h$, it is expected that the flow will be fully-developed. All connections are made leak proof using silicone paste. The entire channel is made of plexiglass for its transparency and therefore good optical access.

Contraction

The area of the square outlet of the centrifugal fan is almost twice as big as the rectangular channel. A contraction is therefore constructed to connect the outlet of the centrifugal fan to the inlet of the rectangular channel. It is labelled B in Figures 3.2 and 3.5a.

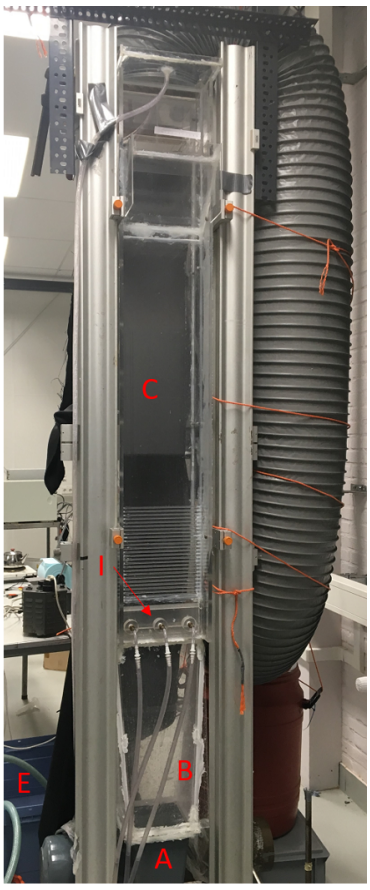

(a)

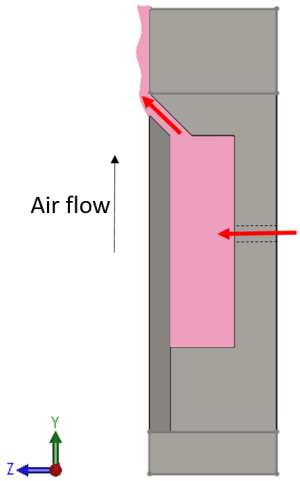

(b)

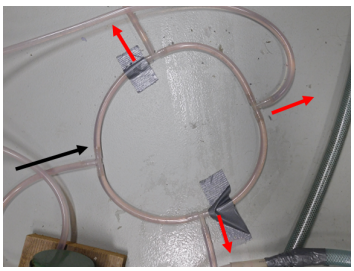

(c)

Figure 3.5: (a) The experimental setup. Labels are the same as in Figure 3.2. (b) The liquid injection box with red arrows indicating the liquid inlet and outlet ports. (c) The distribution of liquid from the pump outlet (black arrow) to the three inlets of the liquid injection box (red arrows).

3.2.2. Liquid Injection

For the creation of a liquid film, an injection system is constructed consisting of a liquid injection box, a pump and a flowmeter.

Liquid Injection Box

The liquid injection box, shown schematically in Figure 3.5b is attached to the cavity containing plate of the rectangular channel. The design of this injection system is inspired by Gill and Hewitt [41], due to its simple design and ease of manufacturing. It has three inlet ports on one side, through which liquid from the reservoir enters the box and an exit slot from which it flows as a film on the channel. The exit slot is inclined at an angle of $45°$ to provide a smooth passage out and prevent adventitious entrainment at the inlet [41]. The three inlet ports are connected to the single discharge of the pump using a tube loop as shown in the Figure 3.5c. The length of the tubes from the loop to the inlet ports are kept equal so that the pressure drop and hence the flow rate through them are equal. The three inlet ports, shown in Figure 3.6, ensure uniform filling of the box.

Figure 3.6: The three inlet ports of the liquid injection box.

Pump

Liquid is drawn from the reservoir and injected into the liquid injection box using a magnetic drive pump (*Iwaki MD 30R*). It has a maximum discharge capacity of $32\ L/min$ and maximum discharge head of $3.8\ m$. To vary the liquid flow rate from the pump, a tap valve is used to coarsely adjust the flow rate. The flow rate is then precisely set by varying the voltage to the pump using a variable autotransformer.

Flowmeter

Flow rate of the injected liquid is measured using a rotameter. A rotameter consists of a float suspended in a tapered tube through which the fluid flows. The position of this float is read from the scale drawn on a glass display. Before using the rotameter, the scale is calibrated by passing liquid with known flow rates through it. Using this calibration, the liquid flow rate can be determined.

3.3. Pitot Tube

As mentioned in Section 3.2, a pitot tube is placed at the fan inlet to ensure a reproducible gas flow rate. In addition to this, it is also used to measure the gas velocity profile at the channel exit. A pitot tube is a slender tube which has two ports: one port is aligned to the direction of the flow and the other port is at the side of the tube. The total and static pressures can be measured using these ports. For an incompressible flow, the Bernoulli's equation is solved to obtain the local velocity:

$$p_{total} = p_{static} + \frac{1}{2}\rho_g U_{g,loc}^2 \qquad \Rightarrow \qquad U_{g,loc} = \sqrt{\frac{2(p_{total} - p_{static})}{\rho_g}} \tag{3.2}$$

In Equation 3.2, p_{total} and p_{static} are the total and static pressure respectively, ρ_g is the gas density and $U_{g,loc}$ is the local gas velocity.

Equipment

The pitot tube is connected to a SETRA 239 pressure transducer to obtain the difference between the total and static pressure. The pressure transducer is connected to a *National Instruments USB-6009* data acquisition board to measure and receive the signal from the transducer. Using the computer software *Labview* from *National Instruments*, the signal is then stored to the computer.

Calibration

To obtain the pressure difference in Pascal, the pressure transducer which gives the output in voltage, needs to be calibrated. The pressure difference is related to the voltage by a linear function given in Equation 3.3:

$$p_{dyn} = c_1 E + c_2, \tag{3.3}$$

where p_{dyn} is the dynamic pressure (difference in the total and static pressures), c_1 and c_2 are the calibration constants and E is the voltage. The calibration is done by selecting some known pressure values in the range of 0 to $2000\ Pa$ and noting the corresponding voltage reading, resulting in the calibration constants $c_1 = 277.1\ Pa$ and $c_2 = 12.5\ Pa$.

Measurement Procedure

The pitot tube measurements are performed at the exit of the channel in the wall-normal and spanwise directions (Z and X directions in Figure 3.1b). For each measurement point, data is acquired for 1 minute with a sampling rate of 100 Hz. In the spanwise direction, the measurements are performed only for half of the channel width due to the practical difficulty in traversing the pitot tube from one end to the other. The velocity profile obtained from this half is mirrored along the centerline to obtain the full velocity profile. It is confirmed that the velocity profile is symmetrical by taking some measurements from the other half as well.

3.4. Laser Induced Fluorescence

A planar laser induced fluorescence (LIF) technique is used to measure the liquid film thickness entering the cavity and the liquid filling in the cavity. Laser induced fluorescence is a non-intrusive, whole field measurement technique which is used to selectively visualize a particular phase in a multiphase system [42]. As the name suggests, LIF uses the emission of fluorescent light, when certain dye molecules are excited by a laser light source. The dye, which is added to the phase to be visualized, should have an excitation spectrum which matches the light source wavelength. The wavelength of the emitted light is different than the excited wavelength and can be selectively captured using an optical filter.

In a typical LIF experiment, a laser beam is converted into a thin sheet of light using a combination of lenses. The sheet illuminates the region of interest, through which the dyed fluid passes. The fluid emits light at a higher wavelength than the laser, which is captured by a digital camera equipped with a high-pass filter.

The dye used in this work is *Rhodamine WT*. It emits light with a wavelength of $\lambda_f \approx 560\ nm$ when excited by a green laser light [43]. The dye concentration is an important parameter, as it is directly proportional to the intensity of the emitted light (considering a locally uniform laser power) [44]. Adding too much dye could lead to total absorption of the light. On the other hand, concentrations that are too low will not result in sufficient contrast. A concentration in the range of 100 to $200\ \mu g/L$ is used to achieve good contrast without total absorption of the light.

The light source used is a Nd-YAG laser manufactured by *Litron Lasers* (*Nano L PIV* model), which emits green light of wavelength $\lambda_l = 532\ nm$. The maximum energy per pulse is $200\ mJ$ for $4\ ns$. A repetition rate of $100\ Hz$ can be obtained from this laser. The initially cylindrical laser beam is converted into a thin sheet of light with the help of a combination of lenses. The emitted fluorescent light is recorded with an *Imager pro X 4M* CCD camera from *LaVision*. The camera sensor has a resolution of 2048×2048, with a pixel size of $7.4\ \mu m$. Although the frame rate specified by the manufacturer is $14\ Hz$, in reality the camera operates at a lower frame rate due to the time taken in the transfer of data from the camera to the computer. The experiments are performed at a frame rate of $8\ Hz$, which is the maximum frame rate for the current experiment setup. The camera body is equipped with a *NIKKOR* $55\ mm$ lens. A high-pass filter is added to the camera lens to allow only the fluorescent light to pass through and blocks the shorter wavelength light from the laser. The camera and laser are operated synchronously using *DaVis 7.2* software from *LaVision*.

Two different LIF experiments are performed in the current work: 1) liquid film thickness measurements, to quantify the thickness of the liquid film that enters the cavity and 2) cavity filling experiments, to study the filling behaviour of the liquid film in the cavities. The two experiments are described in the next sections, where the experimental setup and the settings used, as well as the calibration and post processing steps implemented are explained. First we look into the liquid film thickness measurements, followed by the cavity filling experiments.

3.4.1. Liquid Film Thickness Measurements

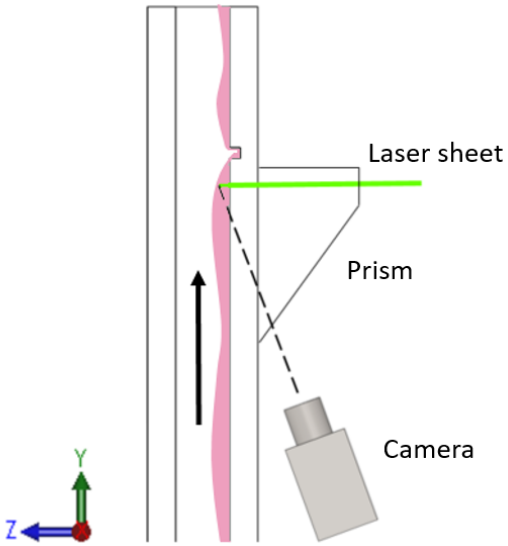

Figure 3.7: Schematic of the setup for the liquid film measurements. Arrow points towards the direction of gas and liquid flow. Laser sheet passes through the prism and illuminates the liquid film, which is captured by a camera. Refractions at the interfaces are ignored.

This section describes the measurements performed to measure the liquid film thickness upstream of the cavity at the chosen flow parameters. A schematic diagram of the setup is shown in the Figure 3.7. The measurement plane is located $150\ mm$ upstream from the upstream cavity edge. The development length for liquid film thickness in upward annular flows as measured by Wolf et al. [45] is $150D$ to $300D$ for a gas Reynolds number based on the tube diameter (Re_D) of 2.5×10^5. However, even for lengths between $13D$ to $15D$ (which corresponds to the lengths of the measurement plane and the upstream cavity edge respectively in the current work), the change in film thickness is only $2.5\ \%$ [45]. Re_{D_h} based on the channel hydraulic diameter in the current work is in the same order of magnitude and so the change is expected to be in the same order of magnitude. Based on this assumption, the film thickness at the measurement plane is considered to be an acceptable measurement for the film entering the cavity.

The laser sheet has a finite thickness due to which the light emitted from the dyed liquid in the streamwise direction (Y-direction in Figure 3.7) also forms a projection on the camera sensor plane. This happens if the angle between the camera view direction and the laser is less than $90°$ and the projection on the camera sensor leads to constant illumination of pixels irrespective of the film thickness, inducing errors in the measurement. This effect diminishes as the angle between the laser and the direction of viewing of the emitted fluorescence increases up to $90°$. However, keeping the angle close to $90°$ can lead to the upper parts of the film to be hidden from the camera due to the curvature of the air-water interface in the Y-direction and therefore leads to an underestimation of the film thickness [46]. Charogiannis et al. [47] suggested that an angle of $70°$ prevents any loss of fluorescence from the top part of the film and gives the best results. Hence our aim here should be to keep the angle

between the laser sheet and the view direction in water to be as close as $70°$ as possible. The camera in the current setup is placed at an angle of $84.5°$ with the laser sheet and a $45°$ prism filled with water is attached to the channel wall. Adding the prism reduces the angle between the incident ray to the camera and the surface normal, causing less deviation of the refracted light. With an angle of $84.5°$, the angle of $74°$ between the laser sheet and the view direction in water is achieved. The prism is also used for calibration of the camera, which is explained in more detail in the upcoming section.

Apart from the error induced due to the finite laser sheet thickness, another source of error is the so called 'mirror effect' due to the total internal reflection of the light emitted from the liquid film, from the out of plane gas-liquid interface [47, 48]. This happens when the emitted light ray strikes the curved interface such that the angle between the interface normal and the incident light is greater than the critical angle ($\theta_c = 48.6°$ in case of air and water at $\lambda_f = 560\ nm$). Looking at Figure 3.8, the rays coming from the bottom part of the film 1 and 2 strikes the interface at a and b respectively at incident angles greater than θ_c. The light ray gets totally reflected and contributes significantly to the light captured by the camera sensor. The intensity of the reflected light is comparable to the intensity of the unreflected light and hence is difficult to distinguish. As a result, the same part 1-2 of the film gets imaged twice and leads to an overestimation of the actual film thickness, which could be as high as 40% [48].

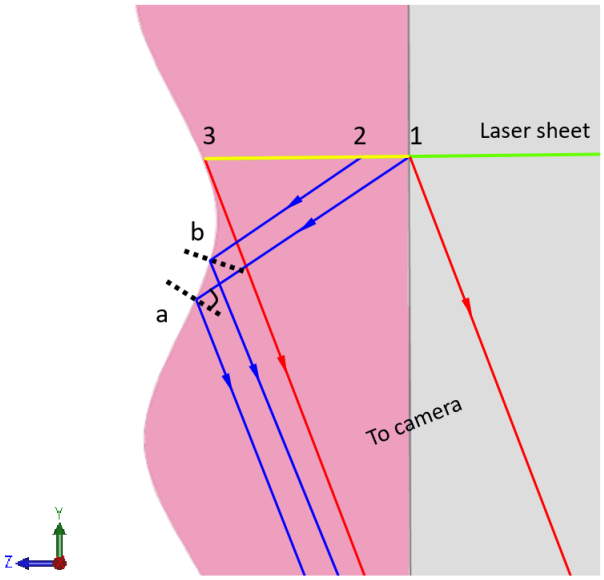

Figure 3.8: The effect of total internal reflection of the emitted light from the gas-liquid interface. Liquid (in pink) is flowing as a film on the channel wall (in gray). The rays from 1 and 2 get totally reflected from points a and b at the interface respectively and contribute to the light captured by the camera sensor.

In this thesis, the overestimated film thickness due to the light ray reflected from 'a' will be termed as the 'uncorrected' thickness, whereas the film thickness due to the unreflected ray from '3' will be called the 'corrected' thickness. To correct for this overestimation, a transparent sheet with vertical line gratings (2 lines/mm) is placed on the outer wall of the channel such that the laser sheet passes through it and creates a structured illumination in the film [47]. This structured illumination can be seen

as vertical lines in the captured image, as shown in Figure 3.9. The unreflected light coming from the film to the sensor appear as straight lines, whereas the reflected light causes the lines to distort. The location of the start of this distortion from the channel wall results in the corrected film thickness. This location is detected in the post-processing step using a MATLAB program.

Settings

To get good quality image data from the experiments, proper settings need to be chosen.

- Magnification ($M_\circ$): The magnification of an optical system is defined as the ratio of the image size and the object size. The size of the camera sensor determines the image size, whereas the object size depends on the required field of view. A field of view with a height/width of $130\ mm$ was chosen so as to image atleast half of the width of the channel. This results in $M_\circ = 0.12$.
- F-stop ($f_\#$): The f-stop of a camera lens is the ratio of the focal length to the diameter of the aperture of the lens. A higher numerical value of $f_\#$ means a smaller opening of the aperture, leading to less light entering the lens and a greater depth of field. The depth of field is the range of distance where the image is in focus. Therefore, an optimum value of $f_\#$ needs to be chosen to get the whole film in focus, with reasonable brightness of the film. The depth of field δz is given as:

$$\delta z = 4.88\lambda_f {f_\#}^2 \left(\frac{M_\circ + 1}{M_\circ}\right)^2 \tag{3.4}$$

A value of 11.2 is chosen for the $f_\#$, which gives a δz of $29\ mm$. The liquid film thickness is expected to be in the order of $1\ mm$ from literature [49], so this focal depth is considered sufficiently high to capture the whole film.

Calibration

The images from the LIF measurement are obtained in pixels and need to be converted to physical units. Calibration is usually done by inserting a target with a grid of markers in the flow domain. The pitch of the markers are known and by taking images of the calibration plate, the pixel values can be converted into length scales. In our experiments, since the calibration needs to be done to know the liquid film thickness, the calibration plate needs to be immersed in water inside the channel. Since it isn't practically feasible to fill the channel with water and insert the calibration plate in it, another method is employed which uses the fluorescence of the dye added to the water in the prism.

A typical raw image recorded from the measurement is shown in Figure 3.9. The region below the red line is illuminated because of the water film on the channel wall. Referring to Figure 3.10, the ray 'c' marks the boundary of this illumination. Within the film, black lines appear because of the structured laser sheet illumination. The physical distance between consecutive lines and therefore the spatial resolution in the X-direction (say in μm/pixel) is known. The region above the blue line is illuminated from the fluorescence of the laser sheet as it passes through the dyed water inside the prism, the boundary of which is marked as 'b' in Figure 3.10. The dark region between the blue and red lines (region b-c in Figure 3.10) is the channel plate. Therefore, from the known physical thickness of the channel plate, the spatial resolution in the Z-direction is known. However, the angle inside the liquid

film would be different from the angle in the channel due to difference in the refractive indices in water and plexiglass. So, the obtained spatial resolution obtained in the Z-direction is corrected for water using the known viewing angle.

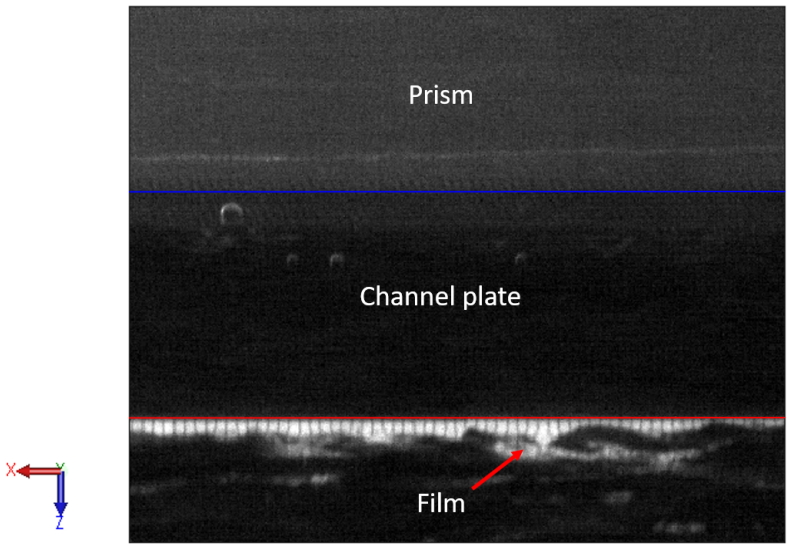

Figure 3.9: A typical image obtained from the measurement. The region below the red line is bright where the liquid film is present. Lines appear in the film due to the structured laser sheet. The region above the blue line is bright due to the presence of dye in the prism through which the laser passes. The channel plate thickness is therefore the region between the blue and red lines.

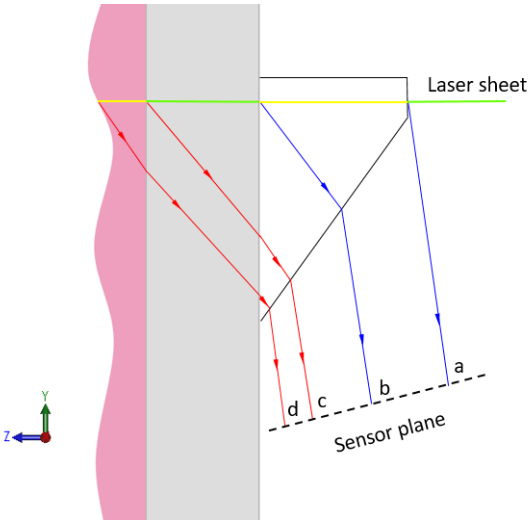

Figure 3.10: A schematic diagram showing the rays that create the Figure 3.9. The blue line at b and the red line at c in the sensor plane represent the corresponding colors in the Figure 3.9.

Measurement Procedure

Liquid in the reservoir is doped with dye such that the solution has a dye concentration of $200\ \mu g/L$. The concentration is chosen on the basis of some trial runs by imaging liquid film with different dye concentrations. The concentration resulting in sufficient contrast in the images (without total absorption of light) is then chosen. The prism is added with water and dye to make a solution with dye concentration of $10\ \mu g/L$. The required gas flow rate is set. The liquid flow rate is then switched on at the highest achievable flow rate to ensure that the channel is fully wet. It is then decreased to the desired rate. The gas flow rate also changes due to the changing pressure drop in the channel and is adjusted. Before starting the recordings, the flow is allowed to reach a state of equilibrium for 5 minutes, as for some cases the channel is observed to be no longer fully wet and a dry patch develops (more on this in Chapter 4, Section 4.3.1). 1000 images are then acquired at a frame rate of $8\ Hz$ for each point in the parameter space to obtain a good value of the mean film thickness.

Post processing Steps

Several post processing steps are implemented to detect first the uncorrected gas-liquid interface and then to detect the location of the lines where they become distorted, which gives the corrected interface. The steps are enlisted and explained with the help of a sample image shown in Figure 3.11:

1. Crop: From the raw image obtained, the position of the channel wall where the liquid flows is detected. The image is then cropped from this wall to a distance of $6\ mm$. This is shown in the top-most Figure 3.11. Although the film thickness is estimated to be in the range of 0.5 to $1\ mm$, a larger margin is chosen to not miss any part of the film. Taking too high a margin, however, leads to higher processing time.

2. Median filter: A median filter is applied to the cropped image to reduce single pixel noise while preserving the edges. A neighbourhood size of 3×3 is chosen with symmetric padding at the boundaries. This results in the second image from the top in Figure 3.11.

3. Contrast stretching: Since the laser sheet intensity is not the same thoughout the measurement plane, the contrast in the liquid film also varies. Another source of contrast variation comes from the fact that the liquid film thickness is not constant and areas of thinner film will be less bright. Therefore, a row-by-row contrast stretching is done in the scale of 0 to 1, which is shown in the third figure.

4. Binarization: The resulting image is then binarized, so that all the pixels above a given threshold is set to 1 and the others to 0. Further, the disconnected parts are removed and the holes are filled. The binarized image before and after removing the disconnected parts and filling the holes are shown in the fourth and fifth image in Figure 3.11. The boundary of this image denotes the uncorrected interface and is plotted on top of the raw image in red, in the bottom-most figure.

5. Line detection: Within the domain marked by the red boundary, the corrected interface is found out by treating each lines individually. For a particular line, the location where it deviates by more than 2 pixels is stored. Plotting these locations for all of the lines results in the blue line in the bottom-most figure, which is the corrected interface.

6. Calibration: The length of the lines are obtained in pixels. Using the calibration steps in the previous section, the pixels are converted into mm.

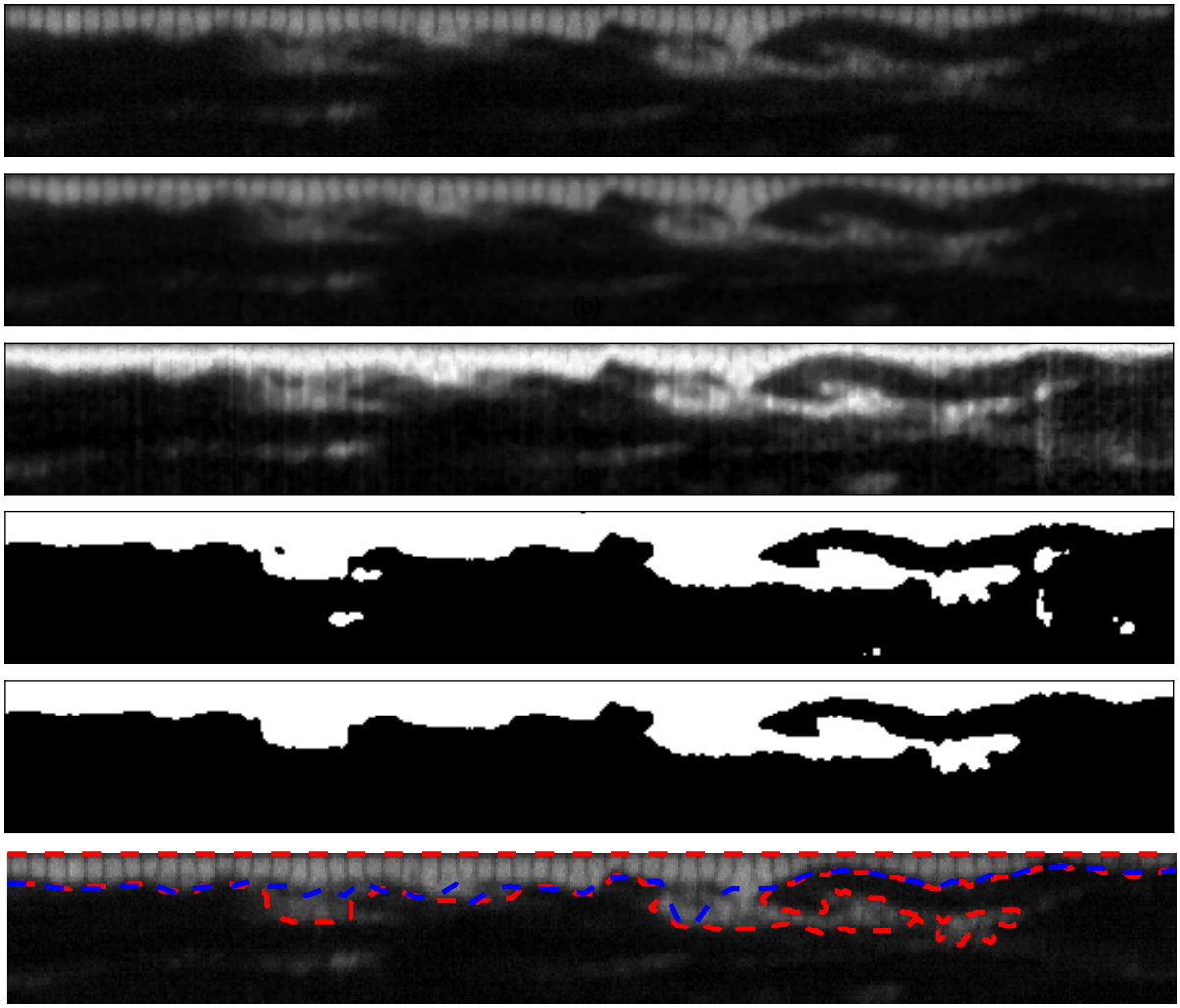

Figure 3.11: The processing steps to detect the interface. From top to bottom: raw image, median filter, contrast streched, binarized, isolated parts removed and holes closed, detection of lines deviating by more than 2 pixels (red is the uncorrected interface and blue is corrected).

3.4.2. Cavity Filling Measurements

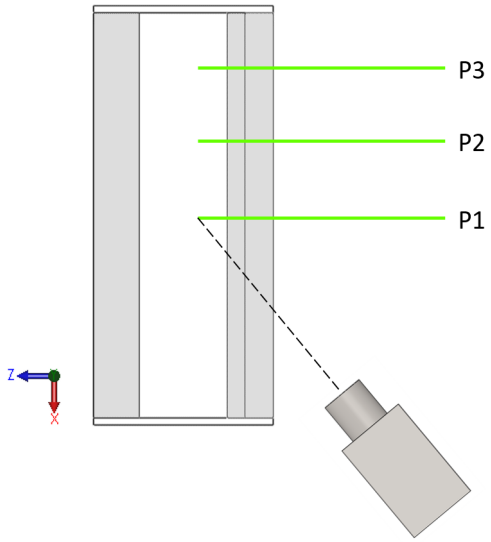

Figure 3.12: Laser sheet and camera position for the cavity filling measurements. The different measurement positions are denoted by P1, P2 and P3. Refractions at the interfaces are ignored.

After the film thickness measurements, the measurements to quantify the cavity filling are performed. The laser sheet is placed in a vertical plane as shown in the Figure 3.12. The camera is positioned at an angle of $35°$ from the laser sheet. The filling is observed to be 3-dimensional, so measurements are performed at three different locations. The first location is at the center of the channel and will be called P1 for the rest of this thesis. The second and third positions are chosen to be $4\ cm$ apart from each other and are denoted as P2 and P3.

Settings

- Magnification ($M_\circ$): Since the camera captured the cavity filling at three different positions, the magnification changes in the range of 0.12 to 0.15.
- F-stop ($f_\#$): The numerical aperture of 11.2 is chosen so as to obtain a depth of field of $29\ mm$. The depth of field being greater than the cavity dimension, is sufficient to have the whole cavity region in focus.

Calibration

The calibration of the cavity filling is done using a similar method as used in the film thickness measurement. The known length and depth of the cavity are used to obtain the spatial resolution in both the directions. Using the camera viewing angle, the spatial resolution is then corrected for water.

Measurement Procedure

As for the film measurements, dye is added to the liquid to make a solution with dye concentration of $100\ \mu g/L$. Gas and liquid flow rates are set to the required value in a similar fashion and 1000 images are captured. After covering all the gas and liquid flow parameters, the position of the laser sheet is changed and the camera is focused to that position. Measurements are then continued similarly.

Post processing Steps

The images acquired from the measurements need to be processed in several steps to quantify the cavity filling. A raw image from the measurement is shown in Figure 3.13a. The red lines mark the boundaries of the cavity. Liquid inside the cavity is seen to be either attached to the cavity walls, or appear as streaks over the cavity. These streaks could either be from out of plane reflections, or from liquid flowing on top of the cavity. However, even if they are actual liquid flowing on top of the cavity, the light emitted from them passes through the liquid present at the cavity bottom and suffer from refractions. As a result, it will appear distorted in shape in the image. Therefore, the objective of this image processing is to remove the streaks and detect only liquid which is in contact with the cavity wall. This is done using the morphological operation called *opening*. It is a combination of two other morphological operations which are *erosion* of an image by a structuring element, followed by its *dilation* using the same structuring element. The different processing steps are explained below.

1. Binarization: The post-processing steps 1 to 4 used in the liquid film measurements are applied to the cavity filling images. That is, a median filter is first applied, followed by row-by-row contrast stretching and lastly, the resulting image is binarized. All the disconnected parts from this binarized image are removed and holes less than 150 pixels are filled. The final binarized image is shown in Figure 3.13b.

2. Erosion: An image erosion step is performed to disjoin the streaks from the liquid attached to the cavity walls. The erosion of an image requires a moving probe matrix called the structuring element. The shape and size of the structuring element determines how it interacts with the image features. Since erosion acts to remove pixel layers from the periphery of the features present in the image, the structuring element determines how these pixels are removed. Its shape and size are often selected empirically, based on the shape and size of the features being treated in the image. From visual inspection of a number of images from the measurement, it is observed that the streaks are connected to liquid attached to the wall by narrow joints of 10-20 pixels in height. A rectangular structuring element of size 13×7 pixels is used first to remove this connection, as shown in Figure 3.13c. Some larger connections are however, still not detached from the liquid on the wall. Therefore, a second erosion step is performed with a structuring element in the shape of a disk of radius 10 pixels. This detaches the bigger features from the liquid present on the cavity wall (Figure 3.13d). A disc is thought to be a suitable choice for this step, as it would erode the features symmetrically from all sides, thereby detaching them. The disjoined streaks after erosion are then removed and only the liquid on the wall is retained, which is shown in Figure 3.13e.

3. Dilation: The erosion step helps to get rid of the unwanted streaks from the image, but it also reduces the size of the features of interest. A dilation step, which is complementary to image erosion is therefore performed. It uses the same structuring element used in erosion, to add pixels to the boundary of the image features. Although the erosion-dilation step is not completely reversible, as erosion removes the finer details and smoothens out the features which cannot be reproduced by the dilation, but it still gives a good representation of the features. From the

image obtained after the dilation step, the boundary of liquid attached to the wall is obtained, which is plotted on top of the original image. The image after dilation is shown in Figure 3.13f. The obtained boundary is shown on top of the original image in Figure 3.13g.

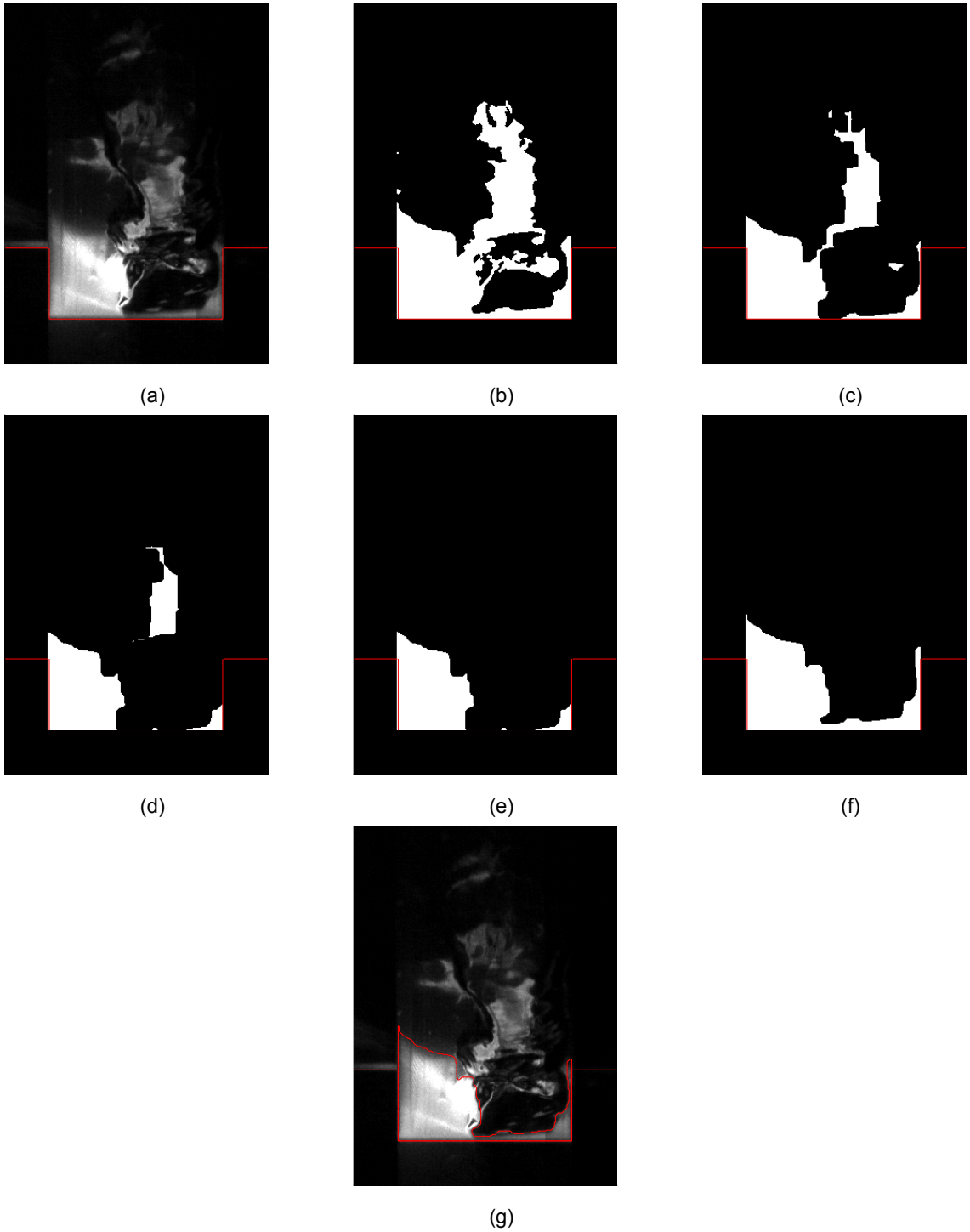

Figure 3.13: Post processing steps implemented to detect the cavity filling. (a) Raw image, (b) binarized image after applying median filter and contrast stretching to raw image, (c) erosion with first structuring element, (d) erosion with second structuring element, (e) the disjoined parts are removed, (f) dilation of the previous image, (g) the boundary obtained from dilated image plotted on top of the raw image.

4

Results and Discussions

4.1. Velocity Profiles

In this section, the results of the gas velocity measurements performed at the channel exit are presented. The measurements are performed using a pitot tube, as explained in Section 3.3. Since the pitot tube measures the local pressure difference (and therefore the local velocity), measurements are required at a number of points across the channel to get a good estimate of the average velocity. The locations of the measurement points across the channel cross-section are shown in Figure 4.1 and tabulated in Table 4.1. The diameter of the pitot tube is $3\ mm$, which limits the measurements near the wall. Velocity measurements in the spanwise direction are only performed for half the channel width, due to practical limitations. Assuming that the velocity profile is symmetric along the center plane, the measured profile is then mirrored along this plane. This assumption was confirmed for one case, where the measurements were performed at both the sides and similar profiles were observed. Typical velocity profiles measured along the wall-normal and spanwise directions are shown in Figure 4.2.

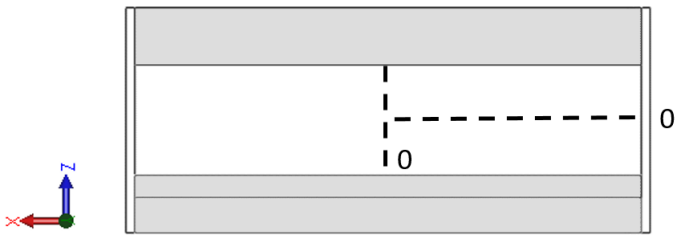

Figure 4.1: Locations of the velocity measurement points. Dotted lines represent traversing locations for the pitot tube. Wall normal direction is the Z-direction in the figure and spanwise is the X-direction.

Along the wall normal direction, the velocity profile is skewed to one side of the channel for all of the

Wall-normal (Z) [cm]	0.25	0.50	0.75	1.00	1.50	2.50	3.50	4.00	4.25	4.50	4.75
Spanwise (X) [cm]	0.30	2.30	4.30	6.30	8.30	9.30	10.30	11.30	11.50	-	-

Table 4.1: Measurement positions in the channel starting from the wall, along the wall normal and spanwise directions.

cases measured. This kind of skewed velocity profile is typical to a centrifugal fan and is attributed to its shell-type shape. The development of the velocity profile from the exit of a centrifugal fan is shown in Figure 4.3a. The measurement plane is located at a distance of $18D_h$, which is greater than the development length of $10D_h$. However, the effect of the fan is still observed.

Along the spanwise direction, the velocity profile shows a local minimum at the center of the channel. Two peaks are observed half-way through the wall before falling off to zero at the channel side-wall due to the no-slip condition. This kind of velocity profile is typically found in axial fans due to the presence of the shaft at the center, as shown in Figure 4.3b. For the centrifugal fan used in the present study, a similar mechanism is expected to cause the observed velocity profile in the spanwise direction. This is because the impeller of the centrifugal fan consists of a hub at the center which reduces the output from there.

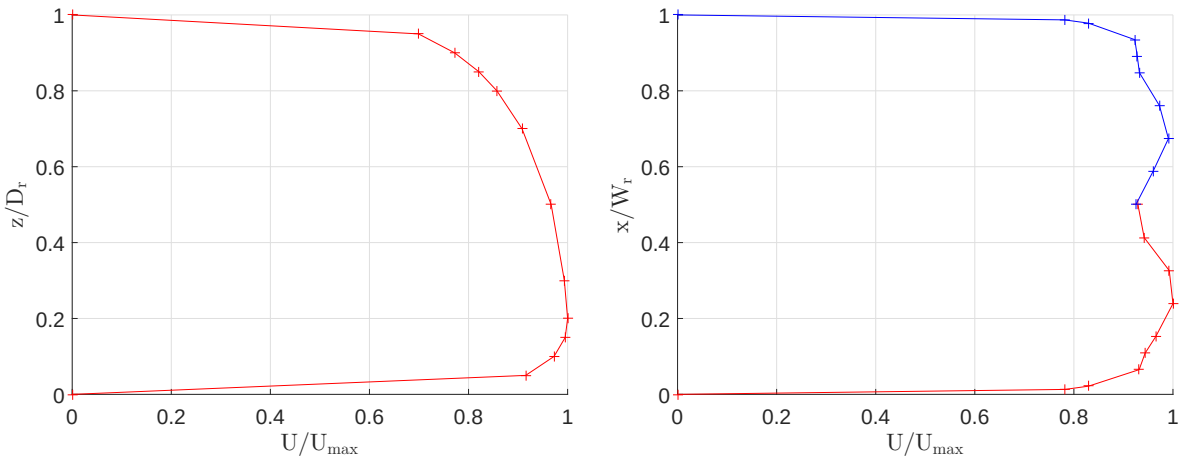

Figure 4.2: Velocity profile at the channel exit obtained from the pitot tube measurement, (a) along wall-normal (Z), and (b) along spanwise (X) direction. The red and blue profiles in (b) correspond to the measurements performed at both halves in the spanwise direction and justifies the similarity assumption.

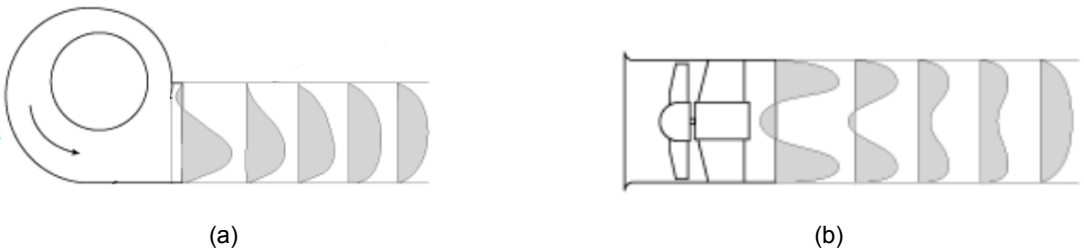

Figure 4.3: Velocity profile development for (a) a centrifugal fan, and (b) an axial fan, adapted from [50].

All the measurements are repeated twice and the velocity is found to vary by 2%. To calculate the bulk gas velocity in the channel, it is assumed that the velocity profiles measured at the center plane along both directions are valid for other lateral positions as well. The following steps are then performed:

1. The velocity in the wall-normal direction is normalized with the maximum velocity in that direction $\left(U_{Z,norm} = U_Z/U_{Z,max}\right)$. The measured velocity profile in the spanwise direction is multiplied with $U_{Z,norm}$, to obtain the corrected velocity at all the lateral planes in the spanwise direction; that is $U_{X,corr} = U_X \cdot U_{Z,norm}$ (the lateral planes are located at the measurement points in the wall-normal direction).

2. The velocity profile along each lateral planes in the spanwise direction is then integrated, to get a single value at the location of these planes (hence the locations of the wall-normal measurements).

3. With these values obtained, another integration step is performed in the wall normal direction, which results in the bulk velocity in the channel.

The bulk velocities measured for different cases corresponding to increasing fan speeds are tabulated in Table 4.2. As mentioned in Chapter 3, a pitot tube is also placed at the fan inlet to measure the velocity at which gas enters the fan. This is used as a control parameter to check the bulk velocity in the channel.

Case	Bulk velocity (U_g) [m/s]
a	16.8
b	19.8
c	23.4
d	27.1
e	29.7
f	30.9

Table 4.2: Gas bulk velocities for the different cases corresponding to increasing fan speeds from a to f.

4.2. Flow Parameters

In this section, the flow parameters at which the measurements are done are discussed. Bulk gas velocities of 25, 27.5 and $30\ m/s$, and liquid flow rates of 0.5, 1, 1.5, 2, 2.5 and $2.8\ L/min$ are chosen. For two-phase flow in cavities, the Weber number (We) is an important parameter, which has already been introduced in Section 2.2. It is the ratio of the inertial force (IN) to the surface tension force (ST) acting on the liquid inside the cavity. The forces are defined in Equation 4.2 [15].

$$We = \frac{IN}{ST} \tag{4.1}$$

$$IN = \rho_g U_j^2 L_j W_r, \qquad ST = \sigma W_r \tag{4.2}$$

In the above equations W_r is the width of the rectangular channel across which the cavity is present and L_c is the length of the cavity. σ is the surface tension for air-water. U_j and L_j are the characteristic velocity scale and length scale for the jet-like gas flow at the downstream edge of the cavity. This flow is the main source of inertial force that acts on the liquid in the cavity. The average velocity of the jet-like flow (U_j) is assumed to be a quarter of the bulk gas velocity (U_g), based on the work of Koschatzky et al. [51] for a flat plate cavity. The characteristic length L_j is taken as one-fourth of the effective cavity length (L_{eff}). The effective cavity length is defined as the length of the cavity free from liquid at half of the cavity depth (see Figure 4.24). It is expected to be around 40% of the geometric cavity length (L_c) based on literature [15], which is also seen in our results presented later in Section 4.5.5 (Figure 4.25).

$$L_j = \frac{L_{\text{eff}}}{4}, \qquad L_{\text{eff}} = 0.4 L_c, \qquad U_j = \frac{U_g}{4} \tag{4.3}$$

Parameter	Range
U_g [m/s]	25, 27.5, 30
Re_{L_c}	1.6×10^4 to 1.98×10^4
Q_l [L/min]	0.5, 1, 1.5, 2, 2.5, 2.8
ϕ_l	2.4×10^{-5} to 1.7×10^{-4}
We	6.4 to 9.3

Table 4.3: Summary of the flow parameters.

The flow parameters are summarized in Table 4.3. For the highest gas flow velocity ($U_g = 30\ m/s$), liquid flow rates greater than $2\ L/min$ could not be achieved, as the additional pressure drop generated due to increasing Q_l could not be overcome by the centrifugal fan.

4.3. Flow Regimes

At the flow parameters mentioned in Table 4.3, three different two-phase flow regimes are observed in the channel: partial film, full film and recirculating film. The partial film regime occurs when the liquid flow rate is low, which results in the formation of a dry patch. At higher flow rates, the channel wall is fully wet and a full film is formed. A recirculating film is observed at the lowest U_g, when the gas flow is unable to balance the injected liquid. A discussion of the observed flow regimes is important, as it affects the liquid distribution in the channel and consequently affects the cavity filling. A description of the dry patch is first presented, followed by the recirculating film.

4.3.1. Dry Patch

At lower liquid flow rates, a partial liquid film is observed, with a dry patch at the middle of the channel wall. An image of the dry patch formed during the experiments is shown in Figure 4.4. This kind of dry patch has been observed and studied before by many researchers [52–54]. The stability of a created

dry patch is generally determined by two approaches. One is the force balance at the stagnation point (point G in Figure 4.5a), as used by Penn et al. [54]. A second approach is the minimization of the total energy of the partial films formed at both sides of the dry patch, as used by Saber and El-Genk [55]. Following the force balance approach on a control volume containing the stagnation point G, as shown in Figure 4.5a, four forces are important. The liquid inertia and shear forces at the liquid-gas interface, which attempt to re-wet the dry patch; and the gravity and surface tension forces, which tends to increase the size of the dry patch. The final force balance therefore reads:

$$\text{Inertia} + \text{Shear forces} = \text{Gravity} + \text{Surface tension} \tag{4.4}$$

Figure 4.4: The dry patch created at the center of the channel wall.

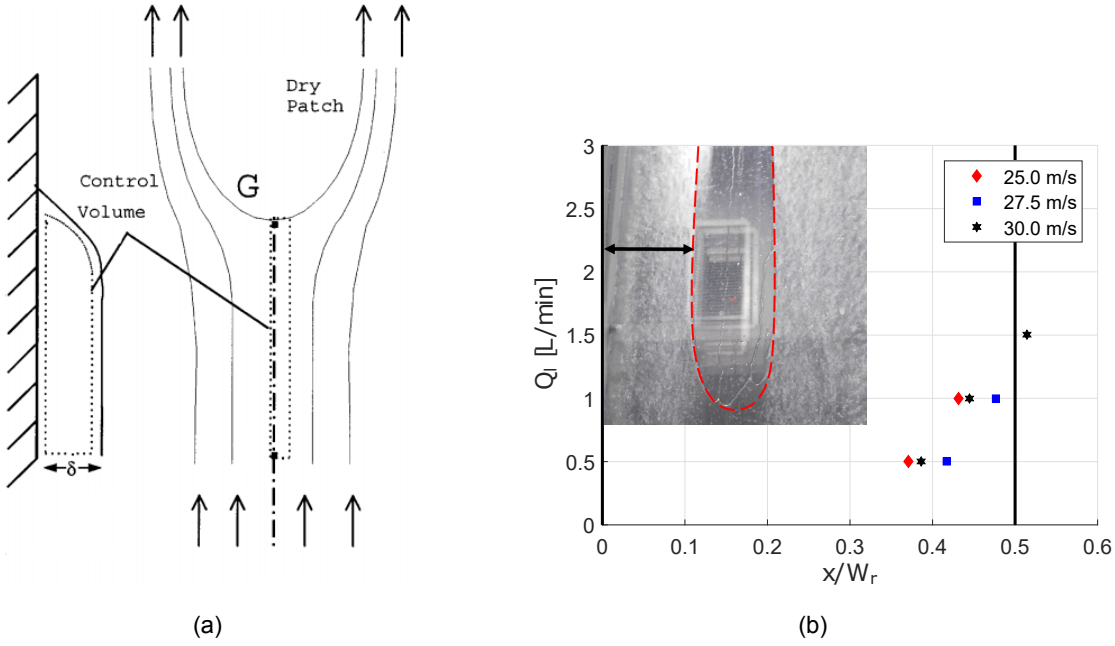

(a) (b)

Figure 4.5: (a) Schematic of a dry patch created for upward gas-liquid flow [54], (b) liquid film width from the side-wall ($x/W_r = 0$). $x/W_r = 0.5$ denotes the center of the channel.

The dry patch reduces in size if the left hand side of Equation 4.4 dominates and grows against the flow direction if the right hand side dominates. At equilibrium, the dry patch remains constant. The measurements are therefore always started after the dry patch has reached its equilibrium size.

For the partial film cases, only one liquid stream could be captured with the camera field of view used in the experiments. The width of the film from the side-wall is plotted in Figure 4.5b. The vertical line at $x/W_r = 0.5$ marks the center of the channel. With increasing Q_l, the dry patch reduces in size and the liquid film becomes wider, as a result of increased liquid inertia. At a certain Q_l, the film for $U_g = 27.5\ m/s$ is the widest, followed by $30\ m/s$ and lastly by $25\ m/s$. This behaviour for $25\ m/s$ occurs due to the recirculating film regime observed, which causes a large part of the liquid to flow at the plate opposite to the liquid injection (see Section 4.3.2). The film for $U_g = 30\ m/s$ is narrower than for $27.5\ m/s$. Referring to Equation 4.4, increasing gas velocity causes an increase in shear forces and liquid velocity, but the film thickness also decreases. If the film thickness falls below the critical thickness, the dry patch is formed. The decrease in film thickness near the center of the channel would be more in case of higher velocity at a particular liquid flow rate, leading to a bigger dry patch.

4.3.2. Recirculating Film

The onset of the recirculating film regime is observed as the gas flow speed is lowered to $25\ m/s$. Unlike the higher velocity cases, where the liquid film flows unidirectionally upward, this regime is characterised by a large amount of liquid recirculating near the side walls. This resembles the transition from churn to annular flow in circular pipes [56]. Taitel et al. [57] suggest that the critical velocity for this transition is related to the minimum gas velocity that is able to suspend the largest stable drop entrained in the gas core. The drop is subjected to a drag force in the direction of the flow and gravity

in the opposite direction. The onset of annular flow occurs when these forces balance:

$$F_d = F_g \qquad \Longrightarrow \qquad \frac{1}{2}C_d(\pi d^2/4)\rho_g U_g^2 = (\pi d^3/6)g(\rho_l - \rho_g) \tag{4.5}$$

$$U_g = \frac{2}{\sqrt{3}}\left(\frac{g(\rho_l - \rho_g)d}{\rho_g C_d}\right)^{1/2}, \tag{4.6}$$

where C_d is the drag coefficient on the drop of size d, ρ_l and ρ_g are the densities of liquid and gas phase respectively. The size of the maximum stable drop ($d_{\max}$) is given by:

$$d_{\max} = \frac{We_c\sigma}{\rho_g U_g^2} \tag{4.7}$$

Combining Equations 4.6 and 4.7 yields Equation 4.8.

$$U_g = \left(\frac{4We_c}{3C_d}\right)^{1/4} \frac{\left(\sigma g(\rho_l - \rho_g)\right)^{1/4}}{\rho_g^{1/2}} \tag{4.8}$$

Here, We_c is the critical Weber number having a value between 20 and 30 for gradually accelerated drops. The value of C_d is taken as 0.44, which is based on the assumption that the drop Reynolds number is in the Newton's law region and is approximately constant [58]. This results in a critical velocity of $15\ m/s$ for the experiments presented in the current study. Therefore if U_g is less than this value, the droplets will fall back. The onset of recirculating flow in the experiments is observed at significantly higher bulk velocities. Recirculation however occurs close to the side wall, where the local gas velocity is lower (Figure 4.2). Due to the recirculation of the liquid, a large amount of liquid is transported to the side walls and the wall opposite to the liquid injection.

The different flow regimes observed at a particular combination of U_g and Q_l are summarized in Table 4.4.

Q_l [L/min]→ U_g [m/s]↓	0.5	1	1.5	2	2.5	2.8
25	R+P	R+P	R+F	R+F	R+F	R+F
27.5	P	P	F	F	F	F
30	P	P	P	F	-	-

Table 4.4: The different flow regimes observed in the measurements. The recirculating fluid regime is marked as R. Cases where a partial film with a dry patch is formed are denoted P and F represents the full film cases. The empty cells denote the parameters where experiments could not be performed.

4.4. Film Thickness

In this section, the results obtained from the film thickness measurements are presented and discussed. The general profile obtained for the liquid film thickness across the channel width is first discussed, followed by the trends of the mean film thickness with the gas and liquid flow parameters.

4.4.1. Typical Film Thickness Profiles

The measured film thickness profile along the width of the channel for $U_g = 25\ m/s$ with $Q_l = 2\ L/min$, which corresponds to the full film case, is shown in Figure 4.6 (left Y-axis). The side-wall is sealed to the channel plate using silicone, which blocks the laser light up to 1 cm (corresponding to $x/W_r = 0.05$ in Figure 4.6) from the side-wall. The film profile therefore starts from $x/W_r = 0.05$ and extends up to $x/W_r = 0.6$, which is defined by the camera field of view in the current setup.

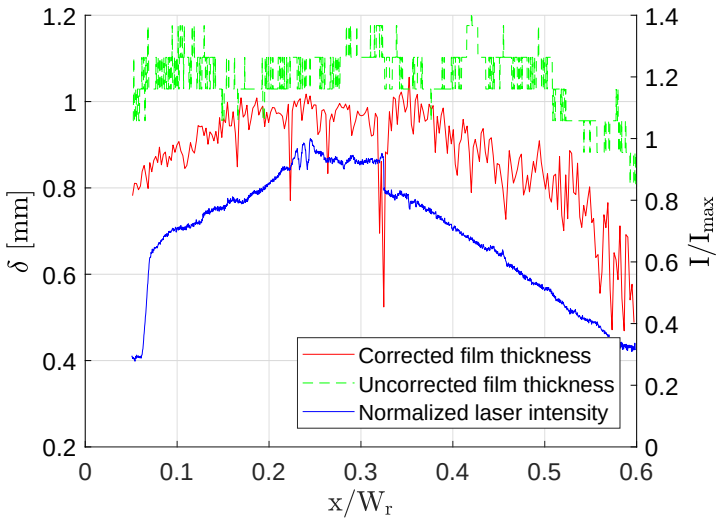

Figure 4.6: The corrected and uncorrected film thickness profile (left Y-axis) and the normalized laser sheet intensity (right Y-axis).

As mentioned earlier in Section 3.4.1, the total internal reflection of light from the gas-liquid interface causes an overestimation of the film thickness, which is corrected in the post-processing steps. An example of the uncorrected film thickness is shown in red in Figure 4.7. It is obtained from the binarization of the image and is plotted on top of the raw image. The average profile obtained using this method is shown in Figure 4.6. The large reflections can be detected using the deviation of the dark lines in the laser sheet. Doing so, a corrected film thickness is obtained, which is also shown in Figure 4.7. The average corrected profile is also plotted in Figure 4.6. From this figure, it is seen that the reflections on average cause a 15% overestimation of the film thickness.

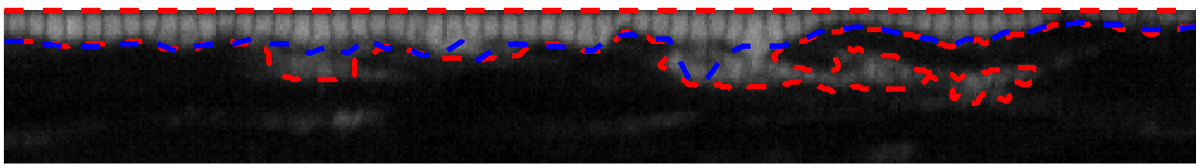

Figure 4.7: The uncorrected interface obtained from the binarized image is plotted in red on top of the raw image. The corrected interface obtained from detecting the deviation of lines is plotted in blue.

The corrected film profile has large dips in thickness, for example at $x/W_r = 0.34$ and between $0.2 \leq x/W_r \leq 0.3$. These dips are due to the changes in contrast in the image acquired by the camera, indicated by the labels a,b,and c in Figure 4.8. The detection of the deviation of the lines depends on the

local contrast changes near a particular line and if there are any lines present in the contrast changing region, its detection becomes difficult and a lower value of film thickness is obtained at that location. The contrast change at $x/W_r = 0.34$, corresponding to location 'a' in Figure 4.8 causes the largest dip in the film thickness and is attributed to the sensor of the camera. Performing dark image correction did not remove this intensity variation from the images. At locations between $0.2 \leq x/W_r \leq 0.3$, smaller dips in thickness are present, which are due to the contrast changes at locations 'b' and 'c' in Figure 4.8. This is due to the presence of bubbles on the prism surface through which the laser sheet passes, blocking the light at those locations.

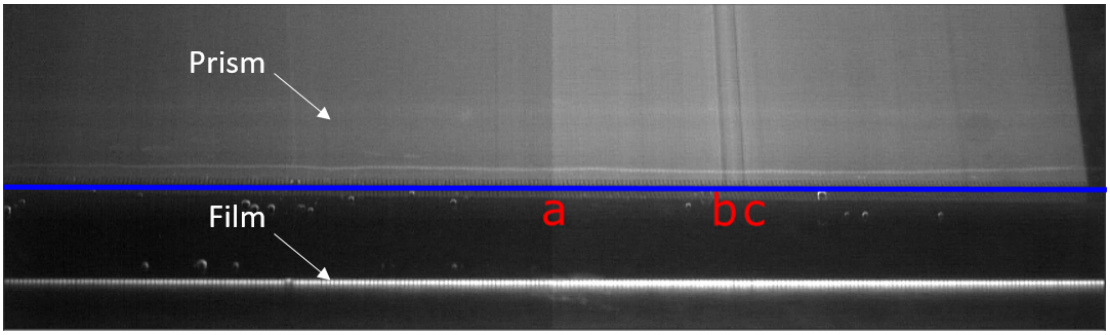

Figure 4.8: The average image obtained by averaging the images for $U_g = 30\ m/s$ with $Q_l = 2\ L/min$. The contrast changes at the center of the image marked 'a' because of the sensor and again at two other locations marked as 'b' and 'c', due to the bubbles present in the prism.

Overall, the corrected film profile has a high thickness at $0.2 \leq x/W_r \leq 0.35$, which drops both towards the side-wall and towards the center of the channel. It was initially thought to be caused by the intensity variation of the laser sheet. The normalized laser sheet intensity is also plotted in Figure 4.6 (right Y-axis). It is obtained from the light emitted from the dyed water in the prism, which is the region above the blue line shown in Figure 4.8. The laser sheet intensity shows a similar profile as the corrected film thickness. However, if the laser intensity variation had an effect on the measurements, this would also show in the uncorrected film profile, since it is obtained directly from binarizing the acquired images. No such correlation is observed between the uncorrected film profile and the laser sheet intensity. Hence, the corrected film profile is believed to be physical rather than a measurement artefact.

The measured profile is attributed to the presence of waves on the liquid film interface. Complex wave structures are observed on the film interface in all the flow regimes. Most notable are the periodic occurence of horse-shoe shaped disturbance waves, as shown in Figure 4.9. The presence of such waves in vertical liquid films sheared by gas flow is well documented in literature [41, 49, 59]. The liquid film flowing at the channel wall is made up of a thin, smooth base film superimposed by rougher disturbance waves [49]. The presence of waves can also be verified from the histogram plot of the film thickness in Figure 4.10, which is positively skewed, similar to the work of Schubring et al. [49].

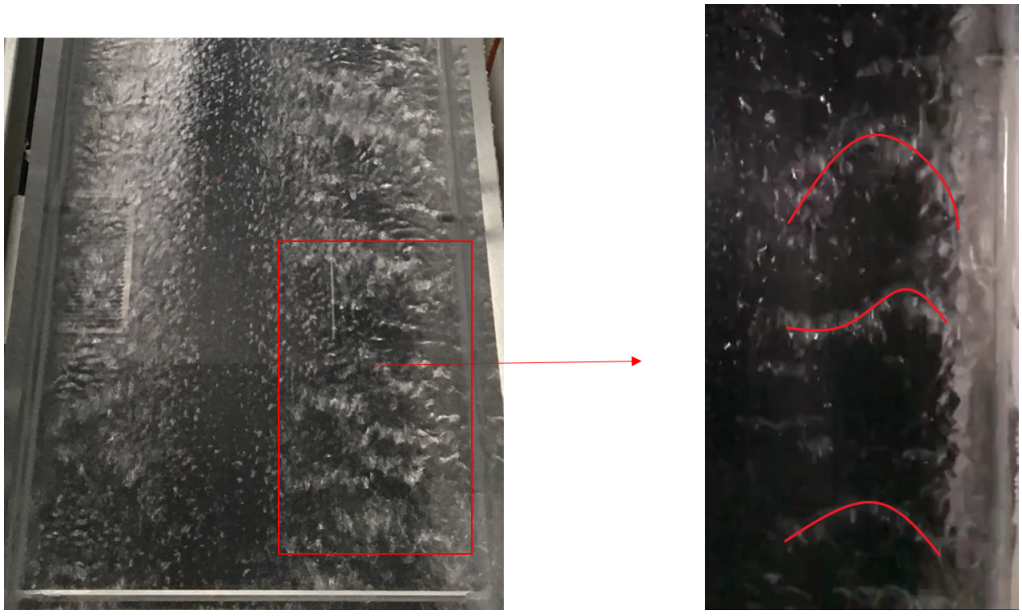

Figure 4.9: Typical wave structures for a full film case (left). At the center of the channel small ripples are observed, whereas close to the side wall disturbance waves occur. The horseshoe shape of these waves is depicted in the right image.

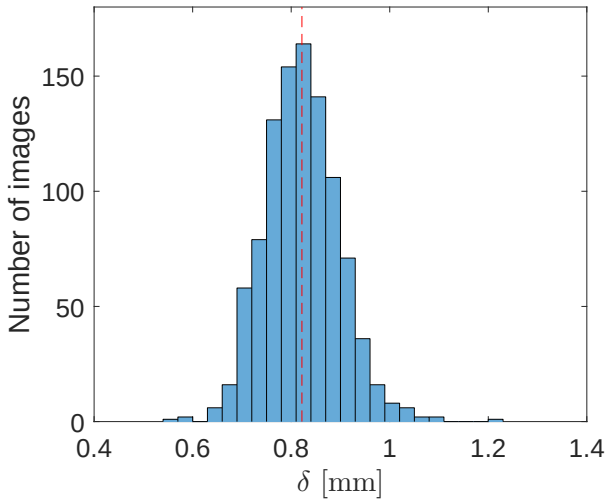

Figure 4.10: Distribution of the film thickness in a measurement series. The distribution has a positive skewness of 0.35. The red line marks the mean film thickness obtained from all the images.

These waves can be generated due to disturbances at the liquid inlet and/or by the perturbation of the gas-liquid interface due to the turbulent gas flow [59, 60]. For the partial film cases, the waves are formed on the liquid films on both sides of the dry patch. Also for the full film cases, the waves do not coherently form across the entire channel width, but are localized similar to the partial film cases, as can be seen in Figure 4.9. It has been shown in circular tubes that the disturbance waves are circumferentially coherent for small diameter tubes, such as that shown by Hewitt and Lovegrove [61] on a tube of internal diameter $32\ mm$; whereas for larger diameters, the disturbance waves are localized as reported by Azzopardi et al. [62] on a $125\ mm$ internal diameter tube. The surface of

the rectangular channel plate can be considered as an infinitely large diameter tube and have such localized disturbance waves. Indeed for liquid films sheared by a gas flow in a horizontal rectangular channel, such localized waves have been reported [63].

The film profile close to the wall, at $x/W_r = 0$ is affected by the presence of the side-wall. This is because of the presence of a viscous boundary layer near the side-wall which causes a decreased wave height [60]. On the right side of the film profile near $x/W_r = 0.6$ in Figure 4.6, the film thickness also decreases. As mentioned earlier, at lower liquid flow rates, the film is partial and a dry patch forms at the center. However, as the liquid flow rate is increased the dry patch gets washed away by a thin and smooth film, causing a decreased film thickness there. With increasing gas velocity, the variation in film thickness along the width increases. This can be seen from the standard deviation plots in Figure 4.11, which are plotted for all three U_g at $Q_l = 2\ L/min$. The standard deviation curves become more concave as U_g is increased. The increase in the concave front as U_g increases is not as significant as the decrease near the center of the channel ($x/W_r \approx 0.5$). This behaviour is expected due to the thinning of the film with increasing gas speeds at a particular Q_l.

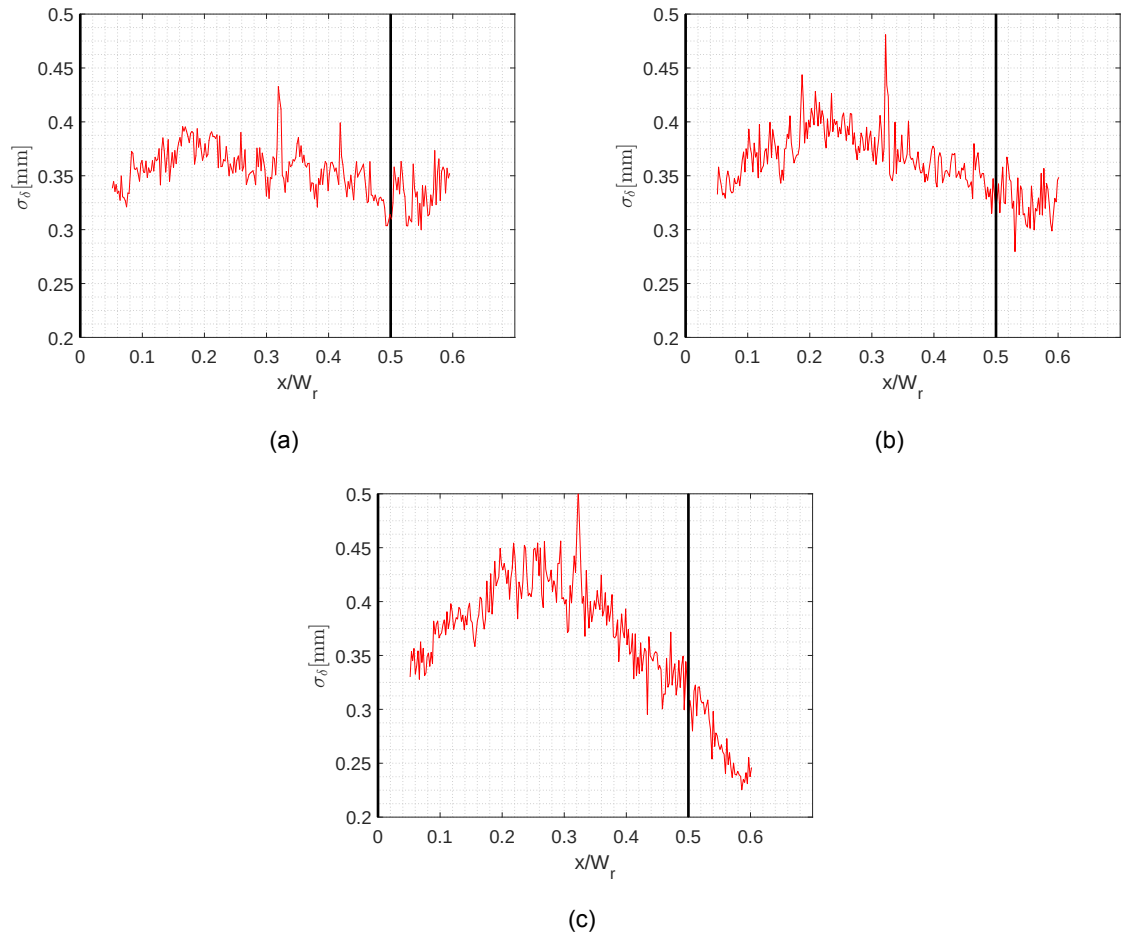

Figure 4.11: Standard deviation in film thickness across the channel width, for $Q_l = 2\ L/min$ with U_g of (a) $25\ m/s$, (b) $27.5\ m/s$, and (c) $30\ m/s$.

4.4.2. Mean Film Thickness

The mean film thickness is calculated by taking the mean of all the data points from the film thickness profile. The mean thickness is expected to increase with the liquid flow rate and decrease with increasing gas velocities because of increased shear stresses at the gas-liquid interface. For the partial film cases, the trends of mean film thickness for all three U_g is shown in Figure 4.12a. No clear trend is observed from this figure. This is because for partial films, the width of the film is also varying. The film area, which is defined as the product of the mean film thickness with the non-dimensional width of the film (x/W_r from Figure 4.5b), is therefore plotted against the liquid flow rate in Figure 4.12b. Open markers represent partial film cases and closed markers represent full film cases.

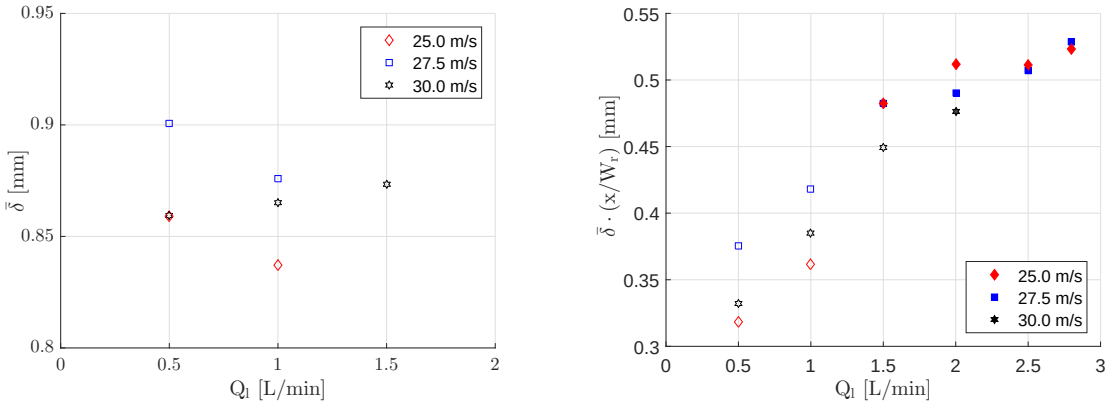

Figure 4.12: (a) Mean film thickness against liquid flow rates for the partial film cases, and (b) film area plotted against the liquid flow rates. Film area is defined as the product of mean film thickness and the non-dimensionalized distance (x/W_r). Open markers represent partial films and closed represent full films.

It is seen from the figure that increasing liquid flow rate causes an increase in the film area for all gas velocities. At a particular liquid flow rate, the trend in the gas velocity for the partial films is similar to that observed for the film width in Figure 4.5b. Therefore, the change in the amount of liquid flowing on the channel wall for partial films is due to its varying width, rather than the change in film thickness. For the full film cases, although plotting the mean film thickness with the flow rate is sufficient, for comparability the film area is plotted together with the area of the partial films in Figure 4.12b. The film area in this case is obtained by multiplying the mean film thickness with $x/W_r = 0.6$, which is the limit of the field of view. The area again increases with an increase in Q_l, however the trend in the gas velocity changes. Especially noticeable is the increase in film thickness for $U_g = 25\ m/s$ from the partial film cases to the full film cases. To better understand this, the film thickness profiles are plotted for liquid flow rate of $1\ L/min$ (partial films) and $2\ L/min$ (full films) for all the gas velocities (Figure 4.14). The film profile is approximated by a fourth order polynomial fit, as shown in Figure 4.13. This is done to reduce noise in the profile and help in the comparison. The partial film profiles are plotted in Figure 4.14a and the full film profiles in Figure 4.14b.

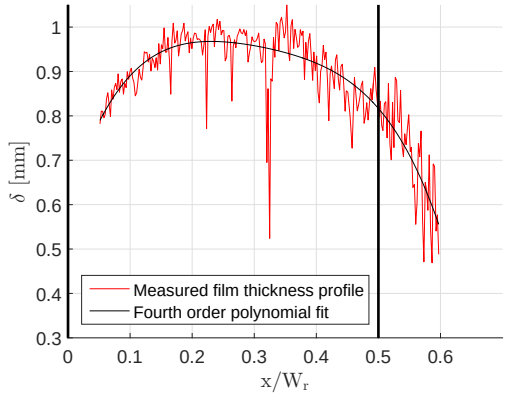

Figure 4.13: Raw film thickness and the fourth order polynomial fit for $U_g = 25\ m/s$ with $Q_l = 2\ L/min$.

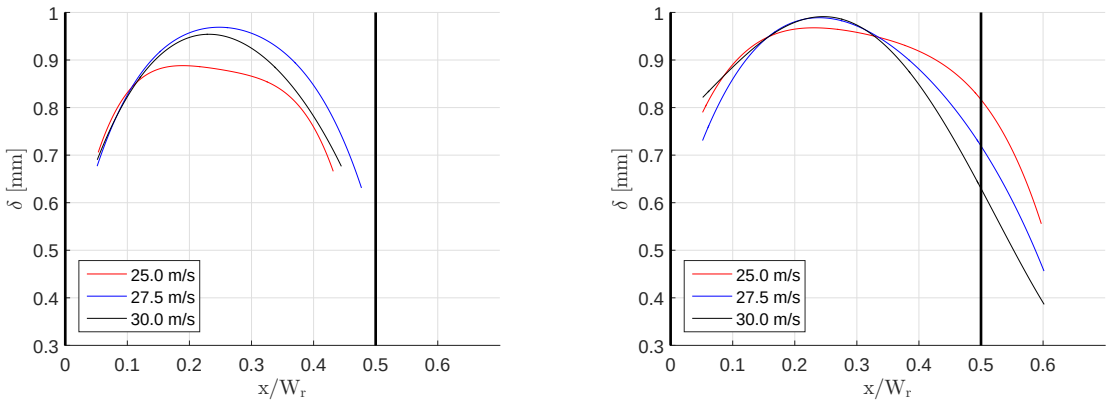

Figure 4.14: The film thickness profile across the channel width for all three U_g with (a) $Q_l = 1\ L/min$, corresponding to partial film cases, and (b) $Q_L = 2\ L/min$, corresponding to full film cases.

For the partial film cases, the film thickness profile for $U_g = 25\ m/s$ is always lower than the other two gas velocities and all three drop to a similar film thickness value before the start of the dry patch at $0.4 < x/W_r < 0.5$. This changes for the full film cases, where an increase in thickness is seen for $U_g = 25\ m/s$ near the former dry patch region around $x/W_r = 0.5$. This causes a higher film area in Figure 4.12b for the full films, as compared to the partial films. Overall, a clear increase in the film area is seen with increasing liquid flow rates, either due to the increase in film width, or due to the increase in film thickness.

4.5. Cavity Filling

After characterizing the liquid film that enters the cavity, its effect on the cavity filling is discussed in this section.

4.5.1. Small Cavities

The measurements were started with small cavities with $L_c = 4\ mm$ and $D_c = 5\ mm$. This geometry falls in the deep cavity classification. Some images were taken to see the filling behaviour in these small-sized cavities. As can be seen from the Figure 4.15, the liquid fills up the cavity completely. From Equation 4.2, we see that the inertial forces (IN) scales with the cavity length. With a smaller cavity length, the inertial force interacting with the liquid inside the cavity is not sufficient to remove it, which causes the liquid to completely fill the cavity. The presence of numerous bubbles can also be observed in the figure. This is also observed in the larger cavity in which the final experiments are done, as shown in Figure 4.16. It was later realized that the water being recirculated in the loop becomes frothy due to the dirty return tubes. Injecting fresh liquid solved this issue, hence for the rest of the experiments fresh liquid was used.

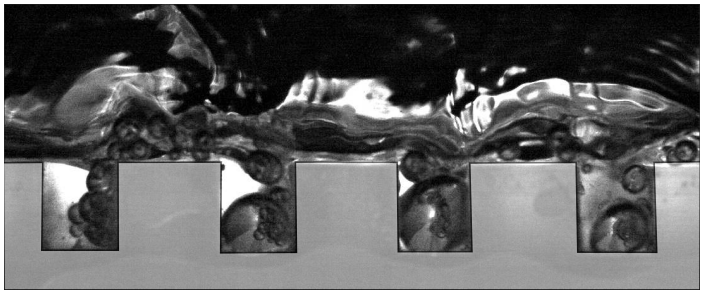

Figure 4.15: Flow over the small cavities used. Flow direction is from left to right, with gravity acting in the opposite direction. The cavities are fully filled with liquid. Numerous small bubbles are present in the cavities.

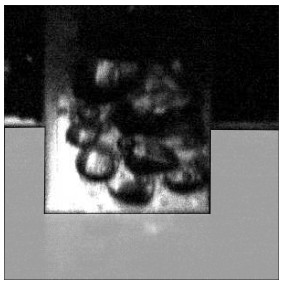

Figure 4.16: Flow over the larger cavity. Bubbles are seen inside the cavity, similar to the smaller cavities used.

4.5.2. Results from the Larger Cavity

The cavity filling measurements are performed at three positions P1, P2 and P3 as shown in Figure 4.17a. The post-processing steps discussed in Section 3.4.2 to detect the liquid accumulation inside the cavity are implemented to all the images. For a particular combination of U_g and Q_l, the processed images are then averaged to obtain a time-averaged filling of the cavity. An example of the time averaged filling profile is shown in Figure 4.17b. This image is subsequently binarized with a threshold of 0.5, resulting in the region bounded by the red line inside the cavity in this figure. This essentially means that only the liquid that is present in the cavity for at least 50% of the time is retained. The flow direction is from left to right and gravity is in the opposite direction.

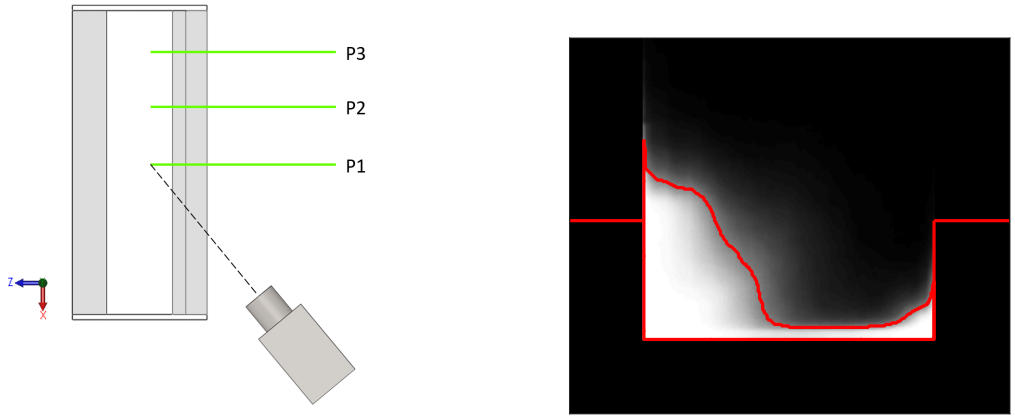

(a) (b)

Figure 4.17: (a) The different positions where the cavity filling was measured, (b) the cavity filling obtained from averaging the post processed images. The red boundary inside the cavity denotes the region where liquid is present for at least 50% of the time.

In Figure 4.18, three different filling ratios in the range of $0.36 \leq \alpha \leq 0.55$ are compared (see Figure 4.19 for the definition of filling ratio). The lower and upper limits of this range correspond to the minimum and maximum filling ratios obtained from the measurements for all the gas and liquid flow parameter combinations. The presence of liquid significantly alters the cavity geometry. A common trait in all the three figures is that the liquid gets displaced and accumulates mostly at the upstream edge of the cavity, similar to the observations of Belfroid et al. [12] and van Eckeveld et al. [15]. Some liquid is present at the downstream cavity edge as well, however it does not vary much with the filling ratio. This can be explained on the basis of the characteristics of cavity flow as discussed in Chapter 2. The shear layer formed at the upstream cavity edge travels over the cavity length and impinges at the downstream edge. Upon impingement a jet-like flow is diverted into the cavity along the downstream wall. This transports any liquid that is present at the downstream wall over the cavity bottom towards the upstream wall. In addition to this inertial force exerted by the gas, gravity also acts in the direction such that the liquid at the downstream edge is dragged towards the upstream wall. At the upstream cavity, the recirculating gas flow shears the liquid and transports it out of the cavity from where it is either entrained in the gas core, or mixes with the passing liquid film and flows over the channel wall downstream of the cavity.

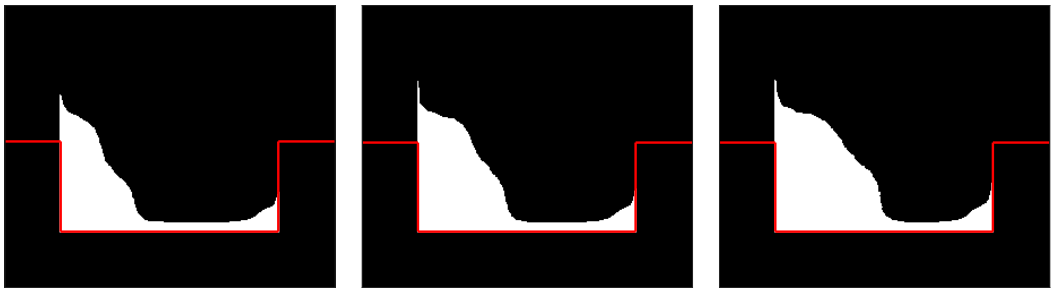

(a) (b) (c)

Figure 4.18: Cavity filling profiles for (a) α = 0.36, (b) α = 0.43, (c) α = 0.55.

The cavity filling behaviour is assessed by quantifying three parameters: filling ratio (α), the effective cavity length (L_{eff}) and the effective cavity depth (D_{eff}). The cavity filling ratio represents the fraction of the cavity area occupied by liquid and is calculated by the total number of white pixels divided by the total number of pixels inside the cavity. The geometrical changes to the cavity are not addressed by the cavity filling parameter. This is important because, as discussed in Chapter 2.6.1, the geometrical changes of the cavity due to the presence of liquid are expected to affect the whistling in corrugated pipes, as shown by van Eckeveld et al. [38]. The cavity length is an important geometric parameter since its ratio with the momentum thickness determines the mode parameter and therefore determines if the flow over cavity will be capable of producing sound. The liquid addition into the cavity decreases its effective length, which could lead to a L_c/θ ratio such that the shear layer mode is not reached. The effective depth of the cavity is another parameter influencing the cavity flow acoustics. The acoustic source strength is dependant on the cavity depth and decreasing the cavity depth has been shown to cause a decrease in the measured sound amplitude [35]. The cavity depth is slightly reduced by the presence of liquid as seen in Figure 4.18.

4.5.3. Filling Ratio

The filling ratio (α) is defined as the ratio of the number of white pixels in the cavity region to the total number of white pixels, as shown in Figure 4.19.

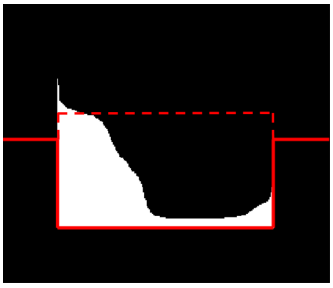

Figure 4.19: The cavity area inside water is marked as red. The filling ratio is defined as the ratio of white pixels to the total pixels inside this area.

The filling ratio for the three positions P1, P2 and P3 is plotted versus Q_l in Figure 4.20a,b and c. Open markers denote the partial film cases, whereas closed markers represent full film cases. For all the positions, an increase in α with Q_l is observed. When comparing the behaviour of α with U_g at P1, with P2 and P3, a difference in the trends is observed. At P1, a lower U_g leads to a higher filling. From experiments done in a corrugated pipe by van Eckeveld et al. [15], it was also observed that the highest corrugation filling occurred at the lowest gas velocity. In a corrugated pipe, the liquid is present on the walls as rivulets or a film which causes a uniform filling of the corrugations over the circumference. An increase in U_g would cause higher shear stresses at the gas-liquid interface leading to lower film thickness and therefore lower filling. Also, the inertial force acting on the liquid inside the cavity would result in a reduced filling at higher U_g. However, for P2 and P3, shown in Figures 4.20b and 4.20c, the trend reverses and the lowest velocity causes the smallest filling. This can be explained by looking at the approximated liquid film thickness profile for $Q_l = 2\ L/min$, shown in Figure 4.20d.

The measurement position P1 is at $x/W_r = 0.5$, whereas P2 is at $x/W_r = 0.33$ and P3 at $x/W_r = 0.15$. At P1, clearly the film thickness for $Ug = 25\ m/s$ is higher than for $U_g = 27.5\ m/s$ or $30\ m/s$. At the other two positions, this trend is reversing causing the filling ratio trends in Figures 4.20b and c.

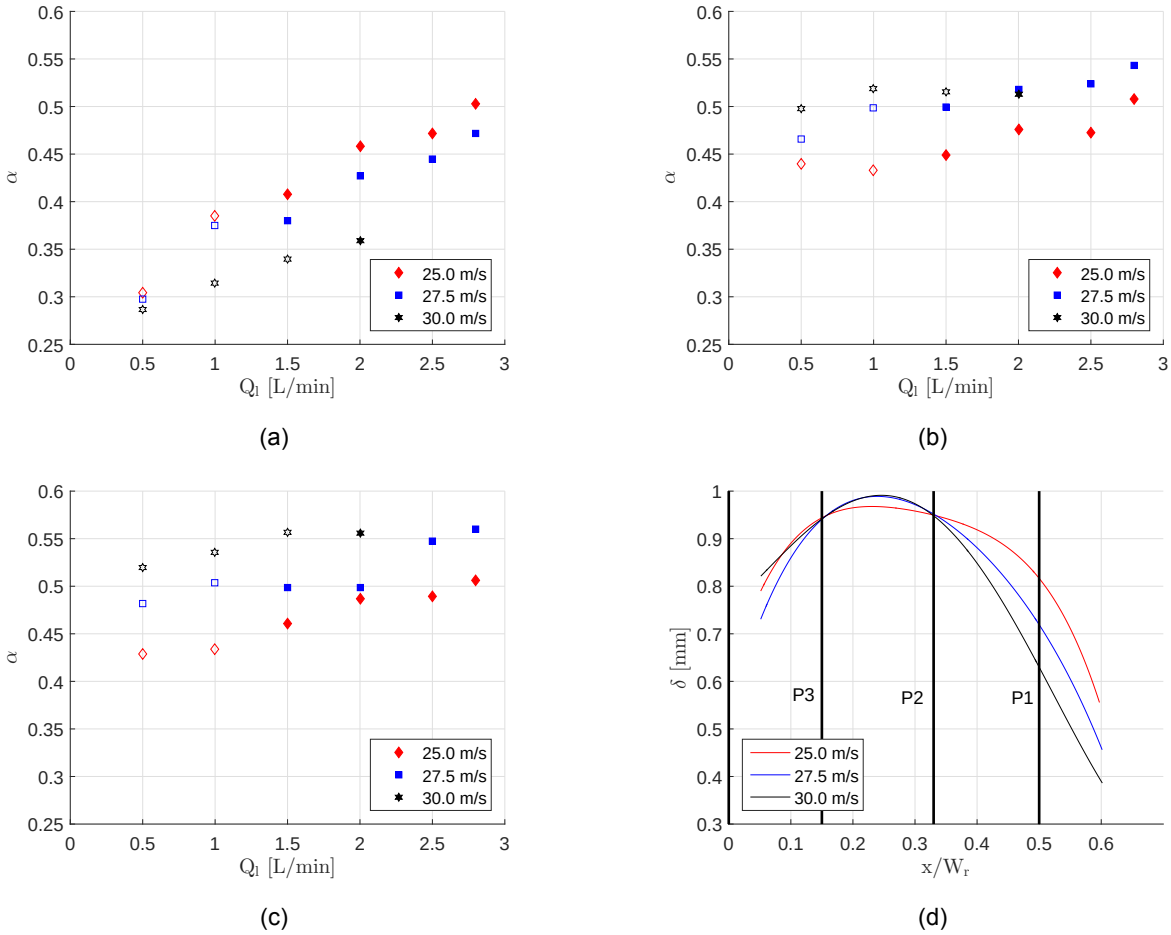

Figure 4.20: The cavity filling ratio (α) plotted against the liquid flow rate (Q_l) for positions (a) P1, (b) P2, and (c) P3. Open markers denote partial film cases, whereas closed markers denote full film cases. (d) Approximated film thickness profiles for all three U_g with $Q_l = 2\ L/min$. Vertical lines at x/W_r = 0.5, 0.33 and 0.15 denote the positions P1, P2 and P3 respectively.

So, it appears that the local film thickness at a particular position affects the measured filling at that position. To confirm this, the filling ratio as a function of local mean film thickness at all three positions is shown in Figure 4.21. Referring to Figure 4.20d, the local film thickness is defined as the thickness value at the intersection of the film profile with the vertical lines denoting the positions. For position P1, it should be noted that only the cases where the film is present on the channel wall at that position are shown (see Figure 4.5b). An almost linear increase in α is observed with the local film thickness at P1. A similar trend is observed at P2 as well, except for the partial film cases for $U_g = 30\ m/s$. At P3, there is a lot of scatter in the data and the trend is less prominent. Since this position is only $3.5\ cm$ from the side walls, flow dynamics inside the cavity can be altered due to this proximity. For a single phase cavity flow, Faure et al. [64] did smoke visualisation experiments on a transverse plane inside the cavity and observed a transverse flow from the side walls towards the center-plane. Another

explanation could be the presence of liquid on the side-walls itself. Since the cavity at the span end is bounded by the side-walls, liquid present there could enter the cavity from the sides.

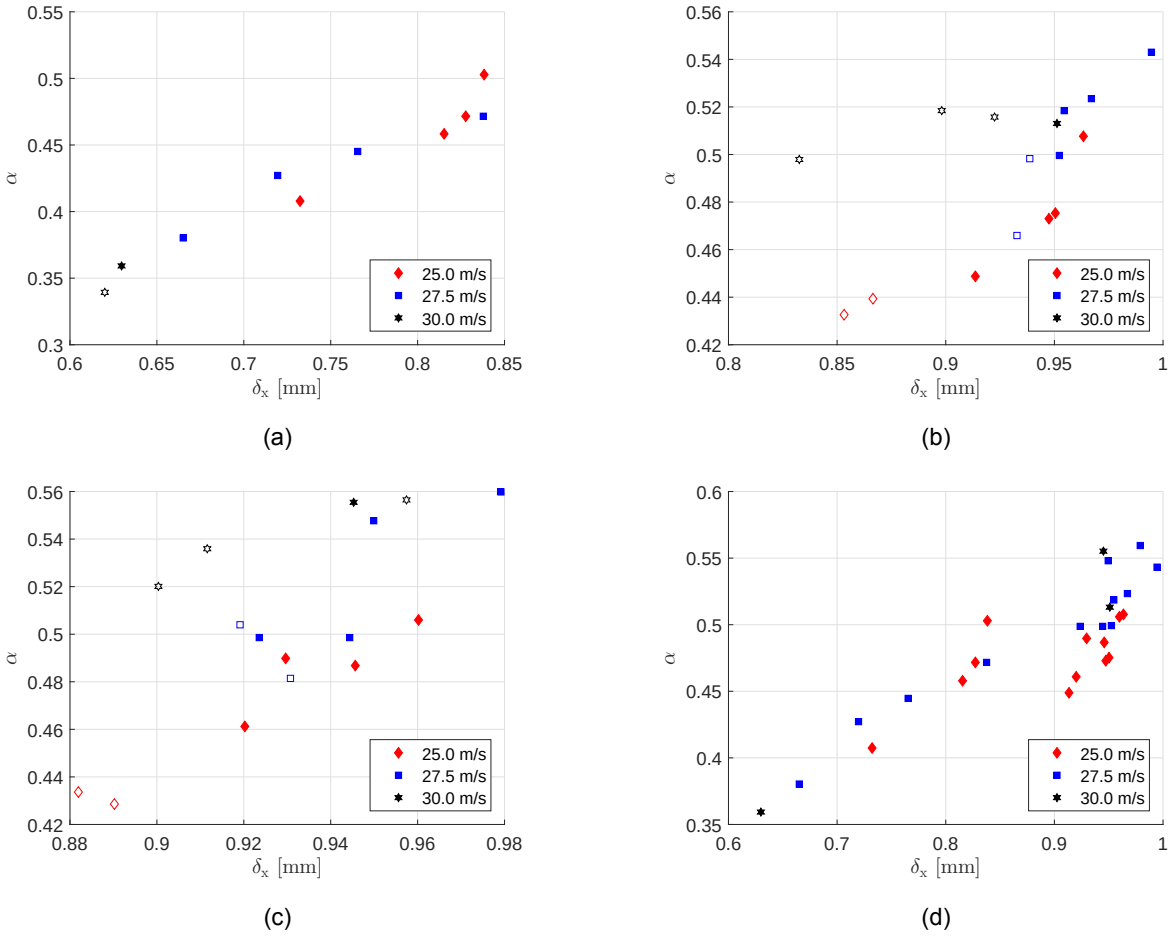

Figure 4.21: The cavity filling ratio (α) as a function of local mean film thickness (δ_x) for positions (a) P1, (b) P2, and (c) P3. (d) Combined for all the three positions for the full film cases.

4.5.4. Effective Depth

The effective depth is defined as the largest empty cavity depth. This is shown schematically in Figure 4.22.

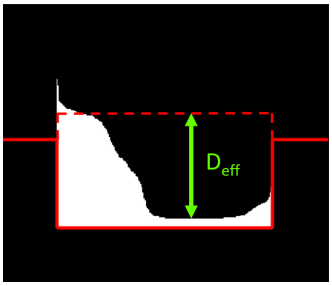

Figure 4.22: D_{eff} is defined as largest empty cavity depth.

The effective depth normalized by the geometric cavity depth (D_{eff}/D_c) is plotted against Q_l for the

three positions in Figure 4.23a, b and c. These plots show that the effective depth does not change significantly with changing flow parameters. This can also be observed qualitatively from the filling comparison at different filling ratios, shown in Figure 4.18. The liquid accumulates at the cavity upstream edge and the effective depth stays relatively constant. In Figure 4.23d, the normalized D_{eff} is plotted as a function of α for all the positions combined. With a 25% increase in the filling ratio, a decrease of only 8% in the D_{eff} is seen.

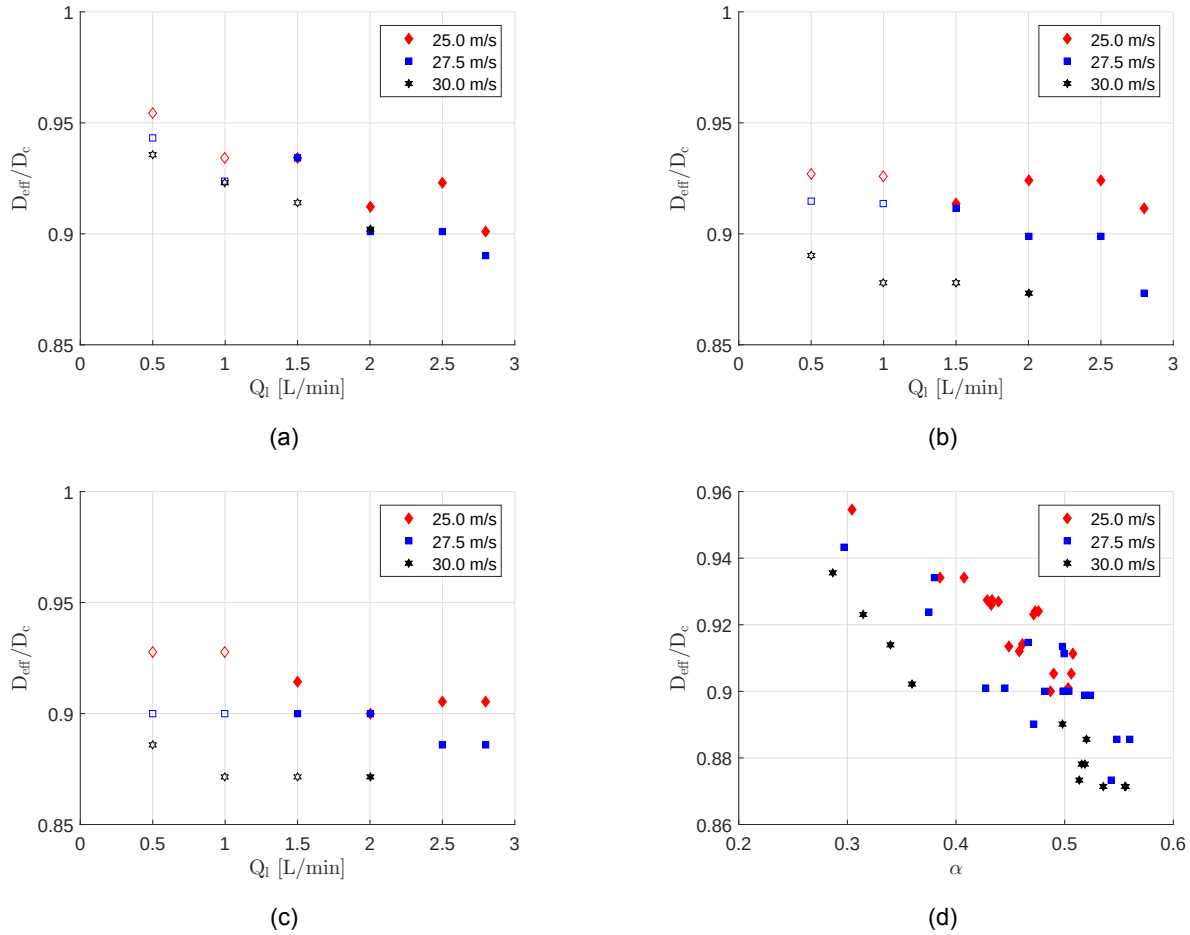

Figure 4.23: The effective cavity depth normalized by the geometric depth (D_{eff}/D_c) plotted against the liquid flow rate (Q_l) for positions (a) P1, (b) P2, and (c) P3. In (d), (D_{eff}/D_c) is plotted against the cavity filling ratio (α).

4.5.5. Effective Length

The effective cavity length is defined as the length of the cavity not occupied by liquid, at half of the cavity depth. The length at half depth is thought to be a suitable choice, since the liquid filling gradually decreases from the cavity bottom to the top. An average change in length can therefore be estimated at half depth.

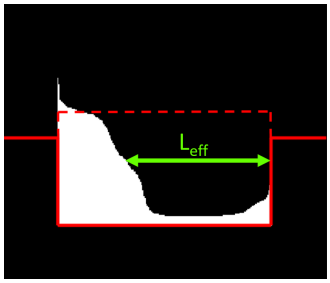

Figure 4.24: L_{eff} is defined as the length of the cavity unoccupied by liquid at half cavity depth.

From the previous two sections, it is seen that varying the flow parameters cause a change in the filling ratio, whereas the cavity depth remains relatively unchanged. It is therefore expected that the effective length of the cavity is strongly affected by the filling. The plots of L_{eff} normalized by the geometric cavity length L_c as a function of Q_l are shown in Figure 4.25a, b and c. Comparing with the filling ratio in Figure 4.20, an inverse relation is seen. That is, a higher filling causes a smaller empty length. The plot of L_{eff}/L_c against α confirm this, where a decrease of 30% in the length is seen with a 25% increase in the filling ratio.

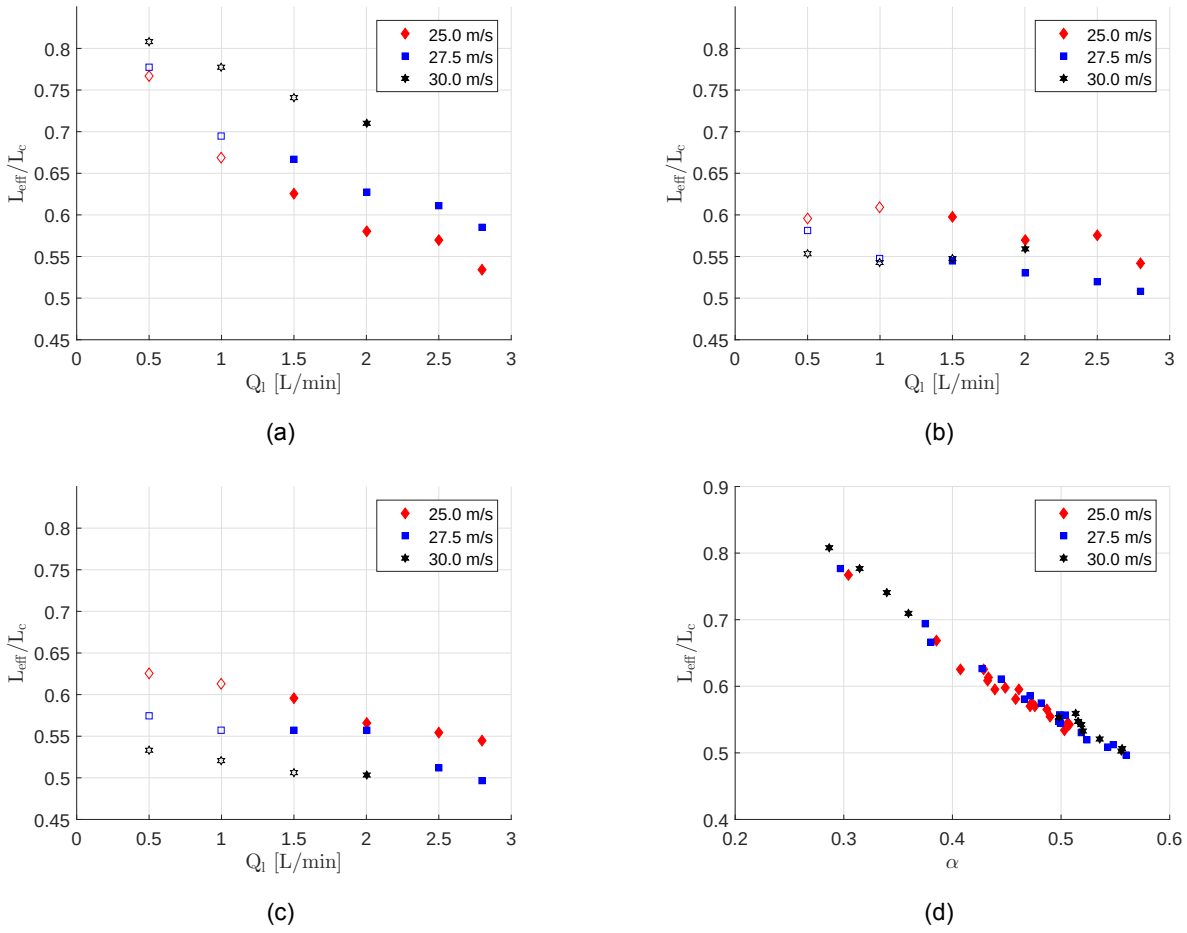

Figure 4.25: The effective cavity length normalized by the geometric length (L_{eff}/L_c) plotted against the liquid flow rate (Q_l) for positions (a) P1, (b) P2, and (c) P3. In (d), L_{eff}/L_c is plotted against the cavity filling ratio (α).

5

Conclusions and Recommendations

In the current work, the effect of a liquid film on the cavity filling is studied experimentally. The filling of the cavities in a flexible riser due to liquid injection is an important mechanism in its whistling mitigation. The flexible riser case is simplified to a rectangular channel test section containing a single cavity. Liquid is injected in the channel, which forms a film at the channel wall and is driven upward by gas flow. Experiments are conducted to measure the thickness of the liquid film entering the cavities and the cavity filling due to this film, using a LIF technique. The main conclusions obtained from this work are summarized in this chapter, followed by recommendations for future research.

5.1. Conclusions

The conclusions drawn from the results are summarized in the following points:

- The gas velocity profiles are measured at the end of the rectangular channel in the wall-normal and spanwise directions, to estimate the bulk velocity in the channel. The velocity profile for the wall normal direction is skewed to one side of the channel, whereas in the spanwise direction, the profile attains a local minimum value at the center-plane and peaks to a maximum value in both directions away from the center-plane towards to side-walls. These profiles corresponds to typical profile obtained from under-developed flow from a centrifugal fan and apparently, more development length is required.
- When a two-phase mixture flows through the rectangular channel, three flow regimes are observed. At lower liquid flow rates, a partial film is created on the channel wall and the central region of the channel is occupied by a dry patch. This dry patch decreases in size and gradually vanishes as the liquid flow rate is increased, creating a full film across the entire channel width. For low gas velocities, a recirculating film regime is observed. The characteristics of this regime

are similar to the churn-annular transition regime. The injected liquid starts recirculating near the side-walls, transporting large amounts of liquid to the opposite wall.

- Measurements for quantifying the liquid film thickness are performed $150\ mm$ upstream of the cavity across the channel width. The film thickness peaks at the center of the measurement plane ($x/W_r \approx 0.2$) and decreases towards the side-wall ($x/W_r = 0$) and towards the channel center ($x/W_r = 0.5$). This profile is attributed to the presence of localized horseshoe shaped disturbance waves on the liquid film surface. An increased wave height is observed at $x/W_r \approx 0.2$, causing the high film thickness measured there. The decrease in wave height near the side-walls leads to a lower film thickness at that location. For the partial film cases, the waves are present across the entire film, but for the full film cases, they are localized and the center of the channel is covered with a relatively thin and smooth film, free from large waves. This causes a reduced film thickness near the center. Overall, the mean film cross-sectional area increases as the liquid flow rate is increased.

- The liquid inside the cavity accumulates near the upstream edge and the downstream edge remains relatively empty. The combined effect of gravity and the jet-like gas flow diverted into the cavity from the downstream edge transports the liquid towards the upstream edge. This creates a negatively sloped gas-liquid interface near the upstream edge.

- The filling measured at a particular position is influenced by the local film thickness at that position. At the measurement position located at the center of the channel ($x/W_r = 0.5$), the filling ratio increases with the film thickness. However, for the position closest to the wall ($x/W_r = 0.15$), the side-wall effects come into play and a clear trend in the filling ratio with the film thickness is not observed.

- The effective depth of the cavity remains relatively constant with increasing filling ratios. A decrease of only 8% is seen with a 25% increase in the filling ratio. The effective length, however is affected significantly. A 25% increase in the filling ratio causes a decrease on 30% in the effective length. Cavity filling is therefore mainly exhibited as an effective shortening of the cavity.

5.2. Recommendations

Some interesting insights on the cavity filling behaviour in the presence of an upstream liquid film are obtained from the current work. Recommendations for future work are enlisted in this section.

- The measured gas velocity profiles did not correspond to a fully-developed flow. An increased development length is required for the flow to become fully-developed. This can be achieved by either increasing the length of the rectangular channel, or decreasing the channel dimensions, resulting in a lower hydraulic diameter.

- Since the carcass of a flexible riser contains a series of subsequent cavities, the filling behaviour of tandem cavities would be interesting to look into. During the current experiments with partial films, it is found that the liquid inside the cavity extended more in the transverse direction than

the width of the liquid film itself. This means that a transverse liquid redistribution occurs within the cavity. The inflow for a subsequent cavity will therefore be significantly altered, causing a different filling in them.

- The effect of the liquid properties such as the viscosity, density and surface tension on the cavity filling would be a relevant extension of the current study. Experiments performed on a flexible riser with different liquids showed different singing behaviour, hinting at a changed cavity filling behaviour [10].

A

Appendix

A.1. Pressure Transducer Calibration

This section shows the calibration of the pressure transducer, which was connected to the pitot tube to measure the velocity profiles at the channel exit (see Section 3.3). Some pressure levels were selected and read from a Betz manometer. The corresponding voltage output from the pressure transducer was noted. The calibration plot is shown in Figure A.1.

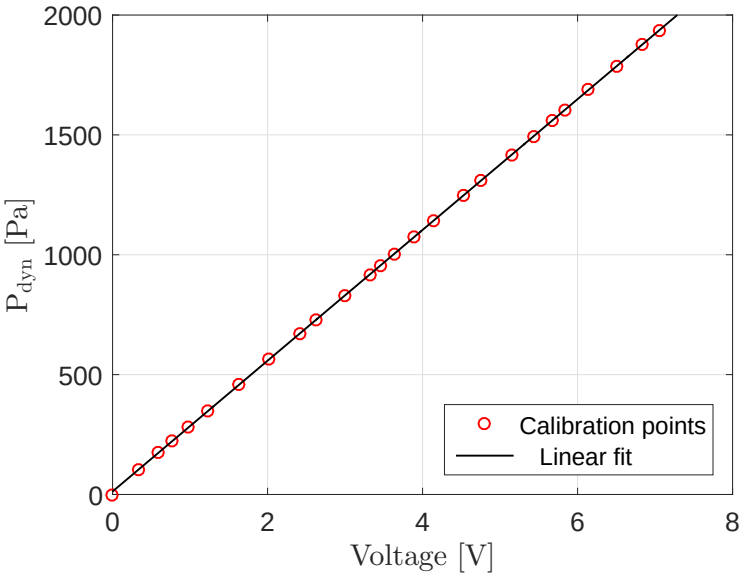

Figure A.1: Calibration of the pressure transducer connected to the pitot tube.

A.2. Rotameter Calibration

The calibration of the rotameter was done is a similar way. The pump speed was varied using a variable autotransformer. The time taken by the pump to displace a certain volume of liquid was noted, giving the liquid flow rate through the rotameter. The corresponding rotameter scale reading was noted, resulting in Figure A.2. Rotameters are generally provided with a linear scale, which is also the seen in our case.

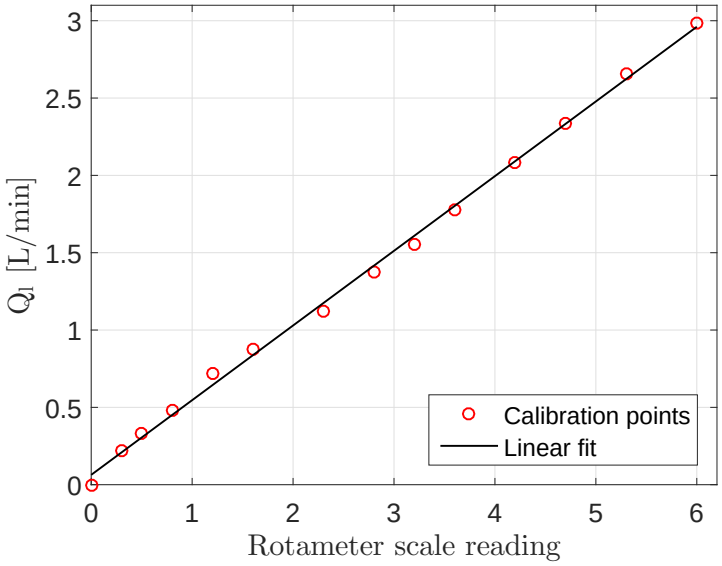

Figure A.2: Calibration of the rotameter.

A.3. Post-processed Images

Some more examples of instantaneous images after the post-processing steps are shown here.

Film Thickness

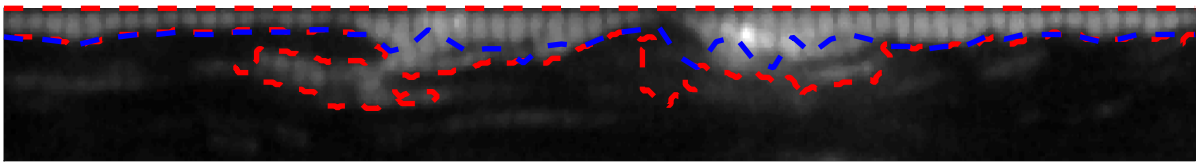

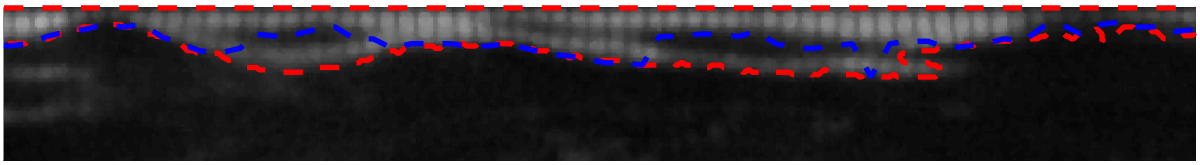

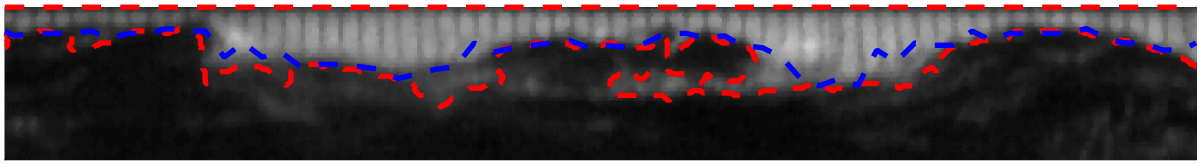

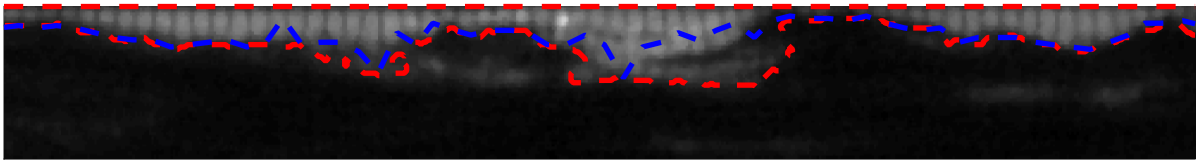

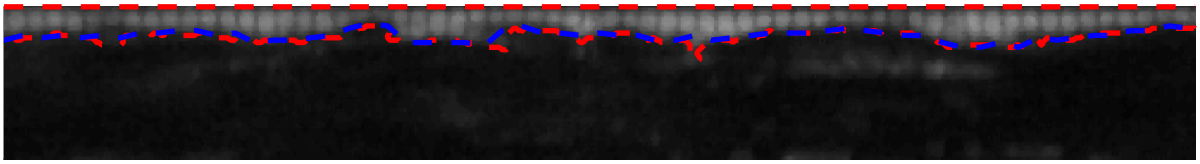

Cavity Filling

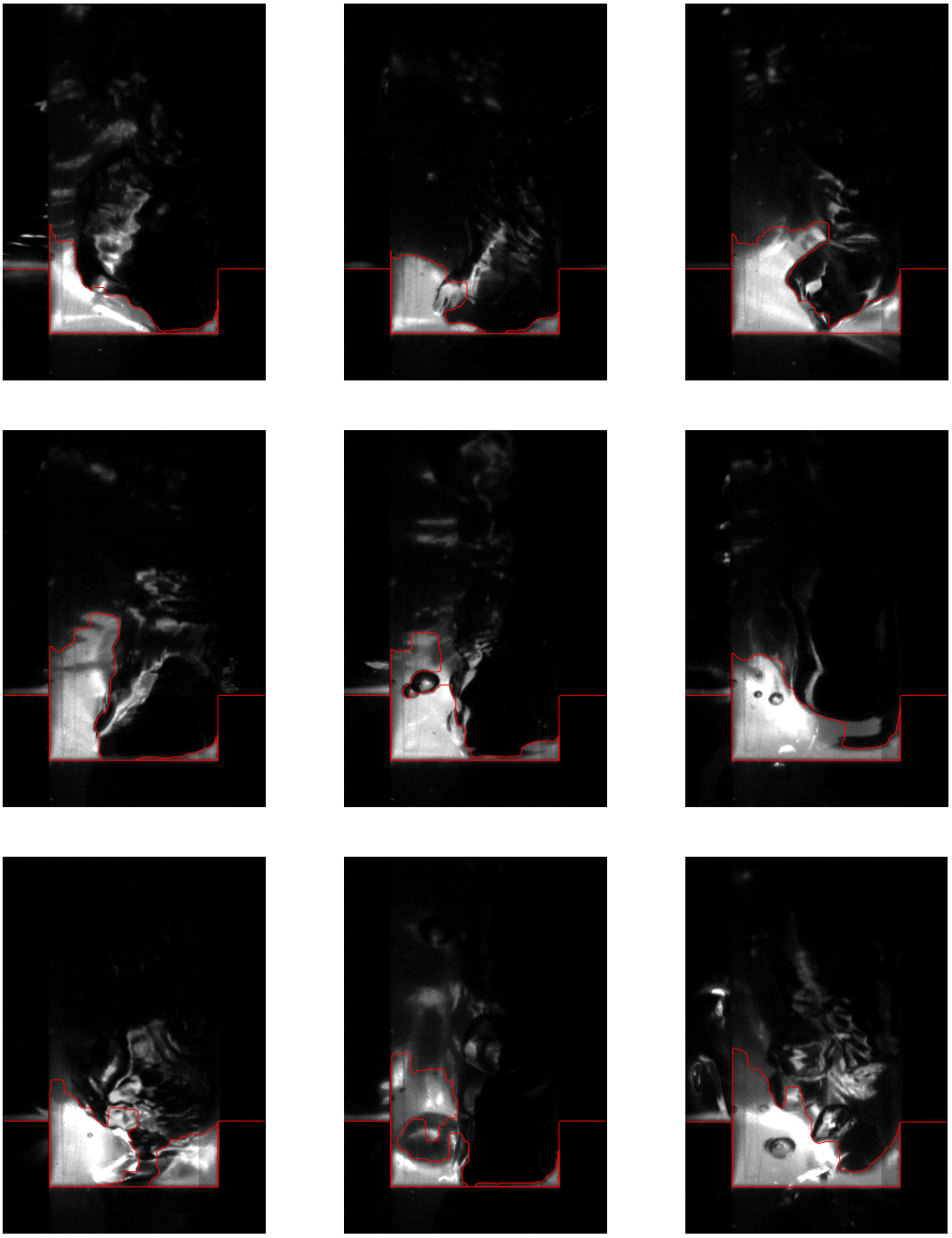

Bibliography

[1] A. Luppi, G. Cousin, and R. O'Sullivan. Deepwater hybrid riser systems. Offshore Technology Conference-Asia, 2014.

[2] Un-bonded flexible risers – recent field experience and actions for increased robustness. ptil.no, 2013. URL http://www.ptil.no/getfile.php/1326003/PDF/Rapporter/4Subsea_%20PSA-Norway_Flexibles-rev5.pdf.

[3] J. Muren. Failure modes, inspection, testing and monitoring. Ptil.no, 2007. URL http://www.ptil.no/getfile.php/135780/PDF/P5996RPT01REV02cSeaflex_JanMuren.pdf.

[4] J.P. Pontaza, B. Abuali, G.W. Brown, F.J. Smith, et al. Flow-induced vibrations of subsea piping: A screening approach based on numerical simulation. In SPE Offshore Europe Oil and Gas Conference and Exhibition. Society of Petroleum Engineers, 2013.

[5] R. Swindell, S. Belfroid, et al. Internal flow induced pulsation of flexible risers. In Offshore Technology Conference. Offshore Technology Conference, 2007.

[6] S. Belfroid, R. Swindell, N. Kitney, et al. Flow induced pulsation of flexible risers. In Offshore Technology Conference. Offshore Technology Conference, 2009.

[7] B. Rajavel and M.G. Prasad. Acoustics of corrugated pipes: a review. Applied Mechanics Reviews, 65(5):050801, 2013.

[8] Y. Nakamura and N. Fukamachi. Sound generation in corrugated tubes. Fluid Dynamics Research, 7(5-6):255–261, 1991.

[9] V. Sarohia. Experimental investigation of oscillations in flows over shallow cavities. AIAA J, 15(7): 984–991, 1977.

[10] S. Belfroid, H.J.C. Korst, P. van Beek, K. Lunde, I.G. Eidsvik, F. Hansen, and B. Olsen. Singing mitigation in an export riser via liquid injection: a field case study. In ASME 2014 Pressure Vessels and Piping Conference, pages V004T04A055–V004T04A055. American Society of Mechanical Engineers, 2014.

[11] Prevention of pulsations in flexibles (risers, flowlines, jumpers), 2013 (accessed September 3, 2017). URL https://www.tno.nl/media/5395/tno_prevention_of_pulsations_in_flexibles.pdf.

[12] S. Belfroid, J. Golliard, and O. Vijlbrief. Singing mitigation in corrugated tubes with liquid injection. In ASME Pressure Vessels & Piping Conference, 2013.

[13] F. Sanna, J. Golliard, and S. Belfroid. On the effect of water film on flow-induced pulsations in closed side branches in tandem configuration. ASME, 2015.

[14] J. Golliard, S. Belfroid, and O. Vijlbrief. Acoustic damping in smooth and corrugated pipes with and without liquid injection. In ASME 2013 Pressure Vessels and Piping Conference, pages V004T04A059–V004T04A059. American Society of Mechanical Engineers, 2013.

[15] A.C. van Eckeveld, J. Westerweel, and C. Poelma. Mitigation of whistling in vertical corrugated pipes by liquid addition. Experiments in Fluids, 58(9):107, 2017.

[16] P.K. Kundu and I.M. Cohen. Fluid mechanics. 2004. Elsevier Acad. Press, London, 199:400, 2008.

[17] Frank M. White. Fluid mechanics. 5th. Boston: McGraw-Hill Book Company, 2003.

[18] Stephen B. Pope. Turbulent flows, 2001.

[19] G.K. Batchelor, H.K. Moffatt, and M.G. Worster. Perspectives in fluid dynamics: a collective introduction to current research. Cambridge University Press, 2002.

[20] University of Western Ontario. Cavity flows, 2017. URL http://www.eng.uwo.ca/people/esavory/cavity.htm.

[21] X. Gloerfelt. Cavity noise. VKI lecture series, 3, 2009.

[22] M. Gharib and A. Roshko. The effect of flow oscillations on cavity drag. Journal of Fluid Mechanics, 177:501–530, 1987.

[23] V. Koschatzky. An experimental study on the aeroacoustics of wall-bounded flows: Sound emission from a wall-mounted cavity, coupling of time-resolved piv and acoustic analogies. 2011.

[24] L. Larchevêque, P. Sagaut, and O. Labbé. Large-eddy simulation of a subsonic cavity flow including asymmetric three-dimensional effects. Journal of Fluid Mechanics, 577:105–126, 2007.

[25] V. Suponitsky, E. Avital, and M. Gaster. On three-dimensionality and control of incompressible cavity flow. Physics of Fluids, 17(10):104103, 2005.

[26] S.C. Morris. Shear-layer instabilities: particle image velocimetry measurements and implications for acoustics. Annual Review of Fluid Mechanics, 43:529–550, 2011.

[27] G. Nakiboğlu. Aeroacoustics of corrugated pipes. PhD thesis, Department of Applied Physics, Eindhoven University of Technology, Eindhoven, The Netherlands, 2012.

[28] X. Liu and J. Katz. Vortex-corner interactions in a cavity shear layer elucidated by time-resolved measurements of the pressure field. Journal of Fluid Mechanics, 728:417–457, 2013.

[29] A.M. Petrie and I.D. Huntley. The acoustic output produced by a steady airflow through a corrugated duct. Journal of Sound and Vibration, 70(1):1–9, 1980.

[30] D.W. Shetler and L.W. Bryson. Vacuum cleaner hose and method for making same, July 19 1994. US Patent 5,330,699.

[31] E. Romero. Flexible corrugated hose and method and tool for reducing noise therin, August 13 1999. US Patent App. 09/374,433.

[32] Y.Y. Pey, L.P. Chua, and W.L. Siauw. Effect of trailing edge ramp on cavity flow structures and pressure drag. International Journal of Heat and Fluid Flow, 45:53–71, 2014.

[33] H.H. Heller and D.B. Bliss. Aerodynamically induced pressure oscillations in cavities-physical mechanisms and suppression concepts. Technical report, Bolt Beranek and Newman Inc Cambridge MA, 1975.

[34] D. Rockwell and E. Naudascher. Self-sustaining oscillations of flow past cavities. Journal of Fluids Engineering, 100(2):152–165, 1978.

[35] G. Nakiboğlu, H.B.M. Manders, and A. Hirschberg. Aeroacoustic power generated by a compact axisymmetric cavity: prediction of self-sustained oscillation and influence of the depth. Journal of Fluid Mechanics, 703:163–191, 2012.

[36] A.C. van Eckeveld, A.K. Pancham, J. Westerweel, and C. Poelma. Flow over partially liquid filled cavity. In 15th European Turbulence Conference 2015 (ETC15), August 25-28th, 2015, Delft, The Netherlands, 2015.

[37] A. Michalke. On spatially growing disturbances in an inviscid shear layer. Journal of Fluid Mechanics, 23(3):521–544, 1965.

[38] A.C. van Eckeveld, J. Westerweel, and C. Poelma. Flow-induced noise in corrugated pipes why does liquid reduce whistling? 2017.

[39] Y.A. Çengel and J.M. Cimbala. Fluid mechanics fundamentals and applications. International Edition, McGraw Hill Publication, 185201, 2006.

[40] R.D. Mehta and P. Bradshaw. Design rules for small low speed wind tunnels. The Aeronautical Journal, 83(827):443–453, 1979.

[41] L.E. Gill and G.F. Hewitt. Data on the upwards annular flow of air-water mixtures. Chemical Engineering Science, 20(2):71–88, 1965.

[42] I. Zadrazil, J.S. An, A. Cherdantsev, and C.N. Markides. Development of LIF techniques applied to gas-liquid annular flows.

[43] J.P. Crimaldi. Planar laser induced fluorescence in aqueous flows. Experiments in fluids, 44(6): 851–863, 2008.

[44] Laser-induced fluorescence LIF, 2017. URL http://web.mit.edu/fluids-modules/www/exper_techniques/3.Laser_Induced_Fluorescenc.pdf.

[45] A. Wolf, S. Jayanti, and G.F. Hewitt. Flow development in vertical annular flow. Chemical Engineering Science, 56(10):3221–3235, 2001.

[46] A.V. Cherdantsev, J. An, I. Zadrazil, and C.N. Markides. An investigation of film wavy structure in annular flow using two simultaneous LIF approaches.

[47] A. Charogiannis, J. An, and C.N. Markides. A novel optical technique for accurate planar measurements of film-thickness and velocity in annular flows. 2017.

[48] T. Häber, M. Gebretsadik, H. Bockhorn, and N. Zarzalis. The effect of total reflection in PLIF imaging of annular thin films. International Journal of Multiphase Flow, 76:64–72, 2015.

[49] D. Schubring, A.C. Ashwood, T.A. Shedd, and E.T. Hurlburt. Planar laser-induced fluorescence PLIF measurements of liquid film thickness in annular flow. Part I: Methods and data. International Journal of Multiphase Flow, 36(10):815–824, 2010.

[50] Understanding fan system effects FA/101-99, 2000. URL http://www.greenheck.com/library/articles/11.

[51] V. Koschatzky, P.D. Moore, J. Westerweel, F. Scarano, and B.J. Boersma. High speed piv applied to aerodynamic noise investigation. Experiments in fluids, 50(4):863–876, 2011.

[52] W. Murgatroyd. The role of shear and form forces in the stability of a dry patch in two-phase film flow. International Journal of Heat and Mass Transfer, 8(2):297–301, 1965.

[53] G.F. Hewitt. The breakdown of the liquid film in annular two-phase flow. International Journal of Heat and Mass Transfer, 8(5):781IN5787–786791, 1965.

[54] D.G. Penn, M.L. de Bertodano, P.S. Lykoudis, and S.G. Beus. Dry patch stability of shear driven liquid films. Journal of fluids engineering, 123(4):857–862, 2001.

[55] H.H. Saber and M.S. El-Genk. On the breakup of a thin liquid film subject to interfacial shear. Journal of Fluid Mechanics, 500:113–133, 2004.

[56] N.H. Taylor and G.F. Hewitt. The motion and frequency of large disturbance waves in annular two-phase flow of air-water mixtures. Chemical Engineering Science, 18(8):537–552, 1963.

[57] Y. Taitel, D. Bornea, and A.E. Dukler. Modelling flow pattern transitions for steady upward gas-liquid flow in vertical tubes. AIChE Journal, 26(3):345–354, 1980.

[58] R.G. Turner, M.G. Hubbard, A.E. Dukler, et al. Analysis and prediction of minimum flow rate for the continuous removal of liquids from gas wells. Journal of Petroleum Technology, 21(11):1–475, 1969.

[59] R.J. Belt, J.M.C. Van't Westende, H.M. Prasser, and L.M. Portela. Time and spatially resolved measurements of interfacial waves in vertical annular flow. International Journal of Multiphase Flow, 36(7):570–587, 2010.

[60] V. Leontidis, J. Vatteville, M. Vlachogiannis, N. Andritsos, and V. Bontozoglou. Nominally two-dimensional waves in inclined film flow in channels of finite width. Physics of Fluids, 22(11):112106, 2010.

[61] G.F. Hewitt and P.C. Lovegrove. Frequency and velocity measurements of disturbance waves in annular two-phase flow. Technical report, Atomic Energy Research Establishment, Harwell (England), 1969.

[62] B.J. Azzopardi, S. Taylor, and D.B. Gibbons. Annular two phase flow in a large diameter tube. Dec 1983.

[63] A.V. Cherdantsev, D.B. Hann, and B.J. Azzopardi. Study of gas-sheared liquid film in horizontal rectangular duct using high-speed LIF technique: Three-dimensional wavy structure and its relation to liquid entrainment. International Journal of Multiphase Flow, 67:52–64, 2014.

[64] T.M. Faure, P. Adrianos, F. Lusseyran, and L. Pastur. Visualizations of the flow inside an open cavity at medium range reynolds numbers. Experiments in Fluids, 42(2):169–184, 2007.